Acta Pharmacologica Sinica

www.nature.com/aps

ARTICLE

3-Hydroxydehydroleucodin ameliorates neuroinflammation and ischemic brain injury by blocking the TRIM21-PRDX1 interaction

Kui Liu[1], Ling Wang[1], Zhuo Chen[1], Yu-xuan Qiu[2], Jia-hong Gao[1], Ting-ting Xie[1], Yue Li[3], He Huang[4], Yang Hu[2]✉, Li-hong Hu[2]✉ and Tao Pang[1]✉

Ischemic stroke triggers profound neuroinflammation and autophagic stress, driven predominantly by microglial overactivation. However, effective therapies targeting this pathogenesis remain elusive. Here, we report the use of 3-hydroxydehydroleucodin (3-Hyd), the primary active component from Kudiezi injection used in China for ischemic stroke patients, as a potent neuroprotective agent that markedly reduces the cerebral infarct area and improves neurological deficits in a mouse model of transient middle cerebral artery occlusion (tMCAO). Integrated bulk RNA sequencing and in vitro assays revealed that 3-Hyd significantly suppressed the microglial proinflammatory phenotype and excessive autophagic flux. Mechanistically, through chemical biology approaches, we discovered that 3-Hyd directly binds to the V51 and R128 residues of peroxiredoxin 1 (PRDX1), which physically disrupts the pathological binding of PRDX1 to its E3 ubiquitin ligase TRIM21, thus preventing the polyubiquitination of PRDX1 at the K109 residue and its subsequent proteasome degradation. Consequently, stabilized PRDX1 impedes TRAF6 ubiquitination, effectively blocking the downstream NF-κB signaling cascade. Strikingly, the anti-neuroinflammatory and cerebroprotective effects of 3-Hyd were largely abolished in microglia-specific *Prdx1* conditional knockdown (*Cx3cr1*$^{Cre/ERT2}$) mice. Together, our findings elucidate a novel TRIM21-PRDX1-TRAF6 signaling axis that governs microglial homeostasis and highlight the pharmacological stabilization of PRDX1 by 3-Hyd to block the binding of TRIM21 with PRDX1 as a promising therapeutic strategy for ischemic stroke.

Keywords: 3-hydroxydehydroleucodin; autophagic flux; microglia; ischemic stroke; PRDX1; ubiquitination.

Acta Pharmacologica Sinica (2026) 0:1–20; https://doi.org/10.1038/s41401-026-01922-6

INTRODUCTION

Stroke is among the leading causes of high morbidity and mortality worldwide [1, 2], with ischemic stroke accounting for 70% to 80% of all acute cerebrovascular diseases. Early restoration of blood perfusion to the ischemic area remains the standard clinical treatment strategy. However, limited by a narrow therapeutic window and low recanalization rates, the process of blood reperfusion often triggers secondary brain injury, namely, cerebral ischemia-reperfusion injury (CIRI), thus further worsening the neurological prognosis of patients [3]. The pathological mechanism of CIRI is highly complex and involves oxidative stress, calcium overload, energy metabolism disorders, and severe immune-inflammatory responses [4]. Among these, neuroinflammation driven by microglia is involved in the initiation, development, and prognosis of CIRI [5–7]. Within minutes after the onset of cerebral ischemia, extensive disruption of the brain tissue structure and damaged neurons release massive amounts of damage-associated molecular patterns (DAMPs), rapidly triggering focal activation of the brain's innate immune system. Although under physiological conditions, microglia possess highly efficient phagocytic and debris clearance capabilities, their phenotypes become abnormal in the pathological microenvironment induced by transient middle cerebral artery occlusion (tMCAO). They undergo severe dysregulation of macroautophagy (herein referred to as autophagy) and sustained pro-inflammatory activation, which in turn exacerbates local brain injury [8–10]. Therefore, rationally and effectively modulating the inflammatory response of microglia to restore their homeostasis is considered a key therapeutic strategy to ameliorate CIRI and promote neurological recovery.

Kudiezi injection (KDZ), a classic traditional Chinese medicine preparation extracted from the Asteraceae plant *Ixeris sonchifolia*, has been extensively investigated for its therapeutic potential in ischemic stroke. Experimental studies using in vivo models have demonstrated that KDZ administration significantly attenuates ischemic injury, primarily by exerting broad-spectrum

[1]State Key Laboratory of Natural Medicines, New Drug Screening and Pharmacodynamics Evaluation Center, China Pharmaceutical University, Nanjing 210009, China; [2]Jiangsu Key Laboratory for Functional Substance of Chinese Medicine, State Key Laboratory Cultivation Base for TCM Quality and Efficacy, School of Pharmacy, Nanjing University of Chinese Medicine, Nanjing 210023, China; [3]State Key Laboratory of Mechanism and Quality of Chinese Medicine, Institute of Chinese Medical Sciences, University of Macau, Macau 999078, China and [4]School of Synthetic Biology and Biomanufacturing, State Key Laboratory of Synthetic Biology, Key Laboratory of Biological and Pharmaceutical Engineering, Tianjin University, Tianjin 300350, China
Correspondence: Yang Hu (huyang@njucm.edu.cn) or Li-hong Hu (lhhu@njucm.edu.cn) or Tao Pang (tpang@cpu.edu.cn)
These authors contributed equally: Kui Liu, Ling Wang

Received: 6 May 2026 Accepted: 13 August 2026
Published online: 09 September 2026

© The Author(s) under exclusive licence to The Shanghai Institute of Materia Medica, Chinese Academy of Sciences and Chinese Pharmacological Society 2026 SPRINGER NATURE

neuroprotective and anti-inflammatory effects [11, 12]. Previous research has shown that KDZ can significantly reduce cerebral infarct volume in mice subjected to middle cerebral artery occlusion and reperfusion (MCAO/R), ameliorate neurobehavioral deficits, and effectively inhibit the expression of pro-inflammatory cytokines such as IL-6, IL-1β, and TNF-α [11, 12]. However, as a complex system composed of multiple components, the specific active material underlying these cerebroprotective effects of KDZ remains to be further elucidated. The main components of KDZ include luteoloside, apigenin, chlorogenic acid, caffeic acid, lupeol, and ursolic acid [13, 14]. Among them, sesquiterpene lactones are key functional components, and 3-hydroxydehydroleucodin (3-Hyd) is among the most promising representatives [15]. Natural products serve as a vital repository of lead compounds for the research and development of innovative drugs [16, 17]. Given the widespread clinical application of KDZ in ischemic brain diseases, elucidating the molecular mechanisms of 3-Hyd—an active component whose biological functions have not been previously reported—will not only help to systematically elucidate the molecular mechanisms of KDZ neuroprotection but also provide highly valuable lead scaffolds for the development of novel targeted drugs against ischemic stroke.

Peroxiredoxin 1 (PRDX1) is a thiol-specific peroxidase that is highly expressed in the central nervous system and plays multidimensional roles in the oxidative stress response, inflammatory network regulation, and tumorigenesis [18]. The regulatory network of PRDX1 is highly dynamic and cell/disease specific and involves multi-level mechanisms such as post-translational modifications, protein–protein interactions, and metabolic reprogramming. For example, transient phosphorylation of PRDX1 at the Tyr194 residue leads to its inactivation and promotes local hydrogen peroxide accumulation [19], whereas its lactylation can inhibit ferroptosis by activating the NRF2 pathway [20]. In recent years, multiple studies have indicated that PRDX1 is considerably involved in the regulation of neuroinflammation in brain diseases [21, 22]; specifically, *Prdx1* knockout leads to severe inflammatory activation in microglia and further exacerbates the infarct volume following cerebral ischemia–reperfusion [23]. Ubiquitination, as a crucial post-translational modification process that determines protein fate and regulates signal transduction, is essential for maintaining cellular homeostasis. However, during the complex pathological progression of CIRI, whether the PRDX1 protein undergoes ubiquitin-dependent degradation, along with its related upstream and downstream regulatory networks, remains unclear. Therefore, systematically elucidating the ubiquitination fate of PRDX1 in stroke disease models and its regulatory effects on microglial function is important.

In this study, using an in vitro neuroinflammation model, we first demonstrated that, compared with other previously reported active components, 3-Hyd is the most potent anti-inflammatory constituent of KDZ. By utilizing multidimensional in vitro and in vivo chemical biology techniques, we comprehensively revealed the target protein of 3-Hyd and its molecular mechanism: 3-Hyd specifically targets the V51 and R128 residues of the PRDX1 protein, thus disrupting the interaction between the E3 ubiquitin ligase TRIM21 and PRDX1, which effectively inhibits the TRIM21-mediated K48-linked ubiquitination and degradation of PRDX1. The stable accumulation of PRDX1 further blocked the TRAF6-mediated activation of the NF-κB inflammatory pathway and the excessive accumulation of autophagosomes. This study not only provides a clear basis and scientific evidence for the clinical application of KDZ but also reveals, for the first time, the critical role of the TRIM21-PRDX1-TRAF6 regulatory axis in microglial autophagy and neuroinflammation, laying a solid theoretical foundation for targeting the TRIM21-PRDX1 interaction in the treatment of ischemic stroke and other neuroinflammation-driven diseases.

MATERIALS AND METHODS

Animals and ethical approval

Cx3cr1$^{Cre/ERT2}$ transgenic mice were purchased from Shanghai Model Organisms Center, Inc. (Shanghai, China). Neonatal mice (postnatal day 1-2) and 8- to 12-week-old wild-type (WT) C57BL/6 J mice were purchased from Jiangsu Huachuang Xinnuo Pharmaceutical Technology Co., Ltd. (Taizhou, China). All animal experiments were approved by the Animal Ethics Committee of China Pharmaceutical University (Approval No.: YSL-202508002) and strictly complied with the National Institutes of Health (NIH) guidelines for the care and use of laboratory animals. Mice were housed under standard conditions (12 h light/dark cycle, 22–24 °C, with ad libitum access to food and water).

Stereotaxic surgery

As described in previous studies [24, 25], mice were fixed on a stereotaxic apparatus (RWD Life Science, China) in a prone position, and anesthesia was maintained with 1% isoflurane. Using a microinjection pump (RWD Life Science, China) with a 30-gauge needle, 1 μL of pAAV-CMV-ZsGreen1-U6-DIO-sh*Prdx1* (5×10^{12} viral genomes/mL) or the control virus pAAV-CMV-ZsGreen1-U6-DIO-shNC (5×10^{12} viral genomes/mL) (both from Cores Biotechnology, China) was injected into the target area of the right cerebral cortex of *Cx3cr1*$^{Cre/ERT2}$ mice (coordinates: 0.5 mm posterior to the bregma, 2.0 mm right of the midline, and 1.0 mm subdural depth) at a rate of 0.05 μL/min. The injection lasted for 20 min, and the needle was left in place for an additional 10 min to prevent liquid reflux. Postoperatively, mice were placed on a heating pad to recover. On day 14 post-surgery, tamoxifen (75 mg/kg; MedChemExpress, HY-13757A) was intraperitoneally injected for 5 consecutive days to induce Cre recombinase expression [26].

Transient middle cerebral artery occlusion (tMCAO) model and the administration of 3-Hyd

A mouse model of tMCAO was induced using the intraluminal suture method, following previously described procedures [27–29]. Briefly, mice were placed in an anesthesia chamber and induced with 2% isoflurane, followed by maintenance with 1% isoflurane (RWD Life Science, China). A midline neck incision was made to expose the right common carotid artery (CCA), and the external carotid artery (ECA) and internal carotid artery (ICA) were carefully isolated. A silicone-coated suture (1800A; Jialing Biotechnology) was inserted through the ECA and advanced into the ICA until reaching the origin of the middle cerebral artery (MCA). After 60 min of ischemia, the suture was withdrawn to restore blood flow and achieve reperfusion. The Sham group underwent the same surgical procedures without suture insertion. During the surgery, the body temperature of the mice was maintained at 37 ± 0.5 °C using a heating blanket.

To explore the effect of 3-Hyd (purity > 98%, provided by Prof. Li-hong Hu's laboratory, Nanjing University of Chinese Medicine) on acute neurological deficits, mice were randomly divided into the Sham group, tMCAO + vehicle control group, tMCAO + 3-Hyd (1 or 2.5 mg/kg) groups and the tMCAO + KDZ (4.8 mL/kg; Shenyang Shuangding Pharmaceutical, Shenyang, China) group. In the *Cx3cr1*$^{Cre/ERT2}$ mice experiment, the mice were randomly divided into six groups: Sham + AAV-shNC, Sham + AAV-sh*Prdx*1, tMCAO + AAV-shNC, tMCAO + AAV-sh*Prdx1*, tMCAO + AAV-shNC + 3-Hyd (2.5 mg/kg), and tMCAO + AAV-sh*Prdx1* + 3-Hyd (2.5 mg/kg). For short-term neurological functional assessment, the vehicle or 3-Hyd was administered immediately at the onset of reperfusion (0 h). For the long-term neurological functional recovery experiment, the administration was performed continuously at 0 h and on 1, 2, 3, 4, 5 and 6 days post-reperfusion. Mice that died unexpectedly during the surgical modeling procedure were excluded from the statistical analysis.

3-Hyd preparation: Dried *Ixeris sonchifolia* (Bunge) Hance herb (200 g) was ground into a fine powder and extracted three times with 10 volumes (mL/g) of 10% aqueous ethanol under reflux, each for 30 min, following a maceration for 1 h at room temperature. The combined extracts were cooled to ambient temperature, centrifuged (4000 × *g*, 15 min), and filtered through qualitative filter paper. The filtrate was then slowly loaded onto a chromatographic column packed with D101 macroporous resin (resin volume = 1.5× the volume of the filtrate) for adsorption. After complete adsorption, the column was sequentially washed with 2 column volumes (BV) of 10% aqueous ethanol to remove sugars, proteins, and inorganic salts. Gradient elution was subsequently performed using 3 BV of 20% aqueous ethanol, followed by 3 BV of 30% aqueous ethanol and 3 BV of 40% aqueous ethanol. Finally, the fraction eluted with 60% aqueous ethanol was collected. This eluate was concentrated to dryness under reduced pressure to afford a crude residue. The residue was further purified by reversed-phase high-performance liquid chromatography (RP-HPLC) on a preparative C18 column, eluting isocratically with 50% aqueous methanol. Compound 3-hydroxydehydroleucodin (3-Hyd, 80 mg) was obtained with a purity >98% (HPLC area %), corresponding to an isolated yield of 0.04% (based on dried herb).

Assessment of cerebral infarct volume and neurological function
As previously described [30], at 24 h post-tMCAO, mice were sacrificed, and the brains were gently removed and sliced into five 1–2 mm thick coronal sections. The sections were incubated in a 2% 2,3,5-triphenyltetrazolium chloride (TTC; Tokyo Chemical Industry, T0520) solution at 37 °C for 15 min in the dark. The infarct area was quantified using ImageJ software (percentage of infarct area = area of the white region on the ischemic hemisphere / total area of the coronal section × 100%). Acute neurological deficits were evaluated using the Longa scoring method. Long-term neurological performance was systematically assessed on 1, 3, 5, and 7 days post-tMCAO using the modified neurological severity score (mNSS) and the rotarod test. All behavioural tests were conducted under double-blind conditions.

Isolation and culture of primary microglia
Following previously described protocols [31, 32], brain tissues were harvested from postnatal day 1 (P1) or P2 neonatal mice and enzymatically dissociated using a papain dissociation system (8 U/mL;) supplemented with 125 U/mL DNase I (TargetMol, T64750). The mixed glial cells were resuspended in DMEM (Gibco, 11965092) supplemented with 10% fetal bovine serum (FBS; Gibco, 10099141) and 1% penicillin–streptomycin (Beyotime Biotechnology, C0222), and seeded at a density of 5×10^6 cells per poly-*L*-lysine-coated T75 flask. After 3 days of culture, the medium was completely replaced with complete medium containing 10 ng/mL GM-CSF (R&D Systems, 415-ML-050). Thereafter, half of the culture medium was changed every 3 to 4 days. After 8 to 10 days of in vitro culture, primary microglia were detached and collected by shaking on an orbital shaker (200 rpm, 2 h). Subsequently, the microglia were harvested every 3 days. The collected cells were seeded at a density of 2×10^5 cells/well in 24-well plates or 4×10^4 cells/well in 96-well plates, respectively, and maintained in a humidified incubator at 37 °C with 5% CO_2 for subsequent experiments.

Isolation and culture of primary bone marrow-derived macrophages (BMDMs)
Based on previously described methods with slight modifications [33–35], BMDMs were isolated from 6- to 8-week-old C57BL/6 J mice. Briefly, the femurs and tibias of the mice were harvested, and the bone marrow cavities were flushed three times with DMEM. The collected bone marrow cell suspension was treated with red blood cell (RBC) lysis buffer (Beyotime Biotechnology, C3702) to remove erythrocytes. Subsequently, the cells were seeded at a density of 5×10^5 cells/mL in DMEM supplemented with 10% FBS, 1% penicillin–streptomycin, and 20 ng/mL M-CSF (Novoprotein, CB34). The cells were induced to differentiate for 6 days, during which the fresh culture medium was replaced every 3 days.

LPS-induced sterile inflammation model
BV2 cells, BMDMs, or primary microglia were pre-treated with the vehicle or various concentrations of 3-Hyd for 2 h, followed by stimulation with 10 ng/mL lipopolysaccharide (LPS; Sigma-Aldrich, L2630) for indicated time periods. Following the treatments, cell culture supernatants were collected for enzyme-linked immunosorbent assay (ELISA), or the cells were lysed to extract proteins and RNA for subsequent analyses.

Oxygen-glucose deprivation/reoxygenation (OGD/R) model
To simulate cerebral ischemia-reperfusion injury in vitro, we established an oxygen-glucose deprivation/reoxygenation (OGD/R) model in BV2 cells. The normal culture medium was replaced with glucose-free and serum-free DMEM (Solarbio Science & Technology, D6540), and the cells were placed in a hypoxic chamber (Billups-Rothenberg Inc., USA) flushed with a gas mixture of 95% N_2 and 5% CO_2 at 37 °C for 2 h. Subsequently, the cells were returned to a standard normoxic environment with complete culture medium and cultured for an additional 12 h of reoxygenation prior to subsequent evaluations.

Bulk RNA-seq analysis
Total RNA was extracted using RNA isolator Total RNA Extraction Reagent (Vazyme Biotech Co., Ltd., R401-01) according to the manufacturer's instructions. RNA purity and quantification were determined using a NanoDrop 2000 spectrophotometer (Thermo Fisher Scientific, USA), and RNA integrity was assessed using an Agilent 2100 Bioanalyzer (Agilent Technologies, USA). Transcriptome libraries were constructed using the VAHTS Universal V10 RNA-seq Library Prep Kit for Illumina (Vazyme Biotech Co., Ltd., NR606-01) according to the manufacturer's protocol.

Differential gene expression analysis was performed using the DESeq2 software. Genes meeting the thresholds of a q-value < 0.05 and a fold change > 2.0 or < 0.5 were defined as differentially expressed genes (DEGs). Hierarchical clustering analysis of the DEGs was performed using R software (version 4.5.2) to demonstrate gene expression patterns across different groups and samples. A radar chart of the top 30 genes was generated using the R package ggradar to illustrate the expression changes of the upregulated or downregulated genes. Subsequently, Gene Ontology (GO) and Kyoto Encyclopedia of Genes and Genomes (KEGG) enrichment analyses of the DEGs were conducted based on the hypergeometric distribution algorithm to screen for significantly enriched functional terms. The significantly enriched functional terms were visualized using R software.

Proteomic sample preparation and target enrichment
To explore the intracellular target proteins of 3-Hyd, BMDMs were lysed using an immunoprecipitation (IP) lysis buffer (Beyotime Biotechnology, P001). The collected cell lysates were incubated with 20 μM of the 3-Hyd-Biotin probe or NP-Biotin (used as a negative control probe) at room temperature for 2 h. Subsequently, the protein complexes were enriched using streptavidin magnetic beads (Cytiva, 28985799). The eluted soluble proteins were precipitated with pre-cooled acetone, washed with methanol, and resuspended in phosphate-buffered saline (PBS) containing 1% sodium dodecyl sulfate (SDS). Then, 2× protein loading buffer was added, and the samples were boiled at 95 °C for 10 min. The samples were separated by 10% SDS-polyacrylamide gel electrophoresis (SDS-PAGE) and subsequently analyzed *via* silver staining (Thermo Fisher Scientific, 24600) or Western

blotting. The differentially silver-stained bands were excised from the gel, destained, and enzymatically digested, followed by identification *via* liquid chromatography-tandem mass spectrometry (LC-MS/MS). The LC-MS/MS analysis and subsequent data processing were performed by OE Biotech Co., Ltd. (Shanghai, China).

Surface plasmon resonance (SPR)

Following previously described protocols [36–38], the binding affinity between 3-Hyd and recombinant human PRDX1 was evaluated in real-time at 25 °C using a Biacore S200 system (Cytiva, USA). After the CM5 sensor chip was activated with a mixture of EDC (75 mg/mL) and NHS (10 mg/mL), recombinant PRDX1 protein (40 μg/mL; Sino Biological, 11194-H08E), diluted in 10 mM sodium acetate buffer (pH 5.0), was covalently immobilized onto the chip surface *via* standard amine coupling chemistry (targeting an immobilization level of approximately 15,000 resonance units [RU]). A blank-activated and blocked flow cell was used as a reference. The binding kinetics assays were performed in 1× HBS-EP running buffer at a flow rate of 30 μL/min. Both the association and dissociation times for the compound were set to 90 s. The data were processed using Biacore Evaluation Software, and the equilibrium dissociation constant (K_D) was calculated by fitting the binding curves using GraphPad Prism software (version 8.0).

Cellular thermal shift assay (CETSA)

Following previously described methods [39, 40], BV2 cells were pre-incubated with 3-Hyd (10 μM) or dimethyl sulfoxide for 2 h. After washing with phosphate-buffered saline (PBS), the cells were harvested, aliquoted, and heated in a dry bath incubator at a preset temperature gradient (43–61 °C) for 3 min, followed by equilibration at room temperature for 3 min. The samples were thoroughly lysed by three repeated freeze-thaw cycles using liquid nitrogen. Subsequently, the soluble supernatants (60 μL) were collected by centrifugation at 13,800 × *g* for 20 min at 4 °C. Finally, 4× protein loading buffer was added, and the samples were denatured by boiling at 95 °C for 10 min prior to Western blotting analysis.

PRDX1 enzyme activity assay and molecular docking simulations

The intrinsic peroxidase activity of recombinant PRDX1 was evaluated using a TRX-TrxR-NADPH coupled assay system, following previously described methods [41]. To predict the interaction mode between the small molecule 3-Hyd and the target protein PRDX1, molecular docking simulations were performed according to previously described protocols [42–44]. The crystal structure of PRDX1 (PDB ID: 4XCS) was retrieved from the RCSB Protein Data Bank (PDB). PyMOL software (version 3.1) was utilized to remove water molecules and original ligands, and to clean the protein structure. Subsequently, AutoDockTools (version 1.5.7) was employed to add polar hydrogen atoms, calculate Gasteiger charges, and convert the protein structure into the PDBQT format. The 3D structure of 3-Hyd was drawn using ChemDraw software (version 20.0) and converted to the appropriate 3D format. The rotatable bonds of the ligand were then defined using AutoDockTools, and the molecule was saved in PDBQT format. A three-dimensional grid box encompassing the predicted binding pocket was generated for the docking calculations. The docking conformation with the lowest binding free energy was selected as the optimal binding pose. Finally, the non-covalent interactions between 3-Hyd and the amino acid residues of PRDX1 were visualized and analyzed using PyMOL software.

Protein–protein docking

In addition to the small molecule-protein docking performed *via* AutoDock, to predict the three-dimensional interaction mode between the E3 ubiquitin ligase TRIM21 and its substrate PRDX1, we employed the information-driven HADDOCK (High Ambiguity Driven protein-protein DOCKing) web server (version 2.4; https://rascar.science.uu.nl/haddock2.4/). First, the crystal structures of the TRIM21 RING domain (PDB ID: 6FGA) and PRDX1 (PDB ID: 4XCS) were retrieved from the RCSB Protein Data Bank (PDB). Water molecules and original ligands were subsequently removed to clean the structures. Following the completion of the online docking calculations, the binding interface and key interacting residues between TRIM21 and PRDX1 were measured and visualized in three dimensions using PyMOL software (version 3.1).

Plasmid construction and siRNA transfection

Human *PRDX1*, *TRIM21*, and *ubiquitin* genes were amplified from a HEK293T cell cDNA library using a high-fidelity PCR kit (Vazyme Biotech Co., Ltd., P526). The amplified fragments were cloned into the pLVX-IRES-Puro vector *via* homologous recombination using a cloning kit (Vazyme Biotech Co., Ltd., C112). Plasmids encoding truncated mutants and site-directed amino acid mutants were also generated using this homologous recombination kit (Vazyme Biotech Co., Ltd., C216). All constructed plasmids were verified as correct *via* Sanger sequencing. The tandem fluorescent mCherry-GFP-LC3B plasmid was purchased from Beyotime Biotechnology (Shanghai, China; Cat. No. D2816). Plasmid transfection was performed using plasmid transfection kit (Polyplus-transfection, 101000006).

For transient transfection and specific gene knockdown, small interfering RNAs (siRNAs) targeting mouse *Prdx1* or *Traf6* (20 nM), or a negative control siRNA (siNC), were transfected into BV2 cells using a transfection reagent (ABclonal Technology, BRK9017-A) according to the manufacturer's instructions. The cells were cultured for 24 to 48 h post-transfection prior to subsequent experiments. The siRNA sequences for *Prdx1* and *Traf6* are listed in Table S1.

Co-immunoprecipitation (Co-IP)

Cells were lysed using a non-denaturing lysis buffer (Beyotime Biotechnology, P001) to extract total proteins. The protein concentration of the whole-cell lysates was adjusted to 1 mg/mL. The whole-cell lysates were incubated with specific primary antibodies, including anti-PRDX1 (Proteintech, 15816-1-AP), anti-FLAG (ABclonal Technology, AE092), anti-HA (Proteintech, 51064-2-AP), or a control IgG (Proteintech, 30000-0-AP) at 4 °C overnight with gentle rotation. The following day, 30 μL of Protein A/G magnetic beads (Selleck Chemicals, B23202) was added to the mixture, which was then incubated for an additional 2 h. The bead-protein complexes were washed five times with pre-cooled lysis buffer, resuspended in 2× protein loading buffer, and boiled at 95 °C for 10 min. The eluted proteins were subsequently analyzed by Western blotting.

Western blotting analysis

Total proteins were extracted from cell or tissue samples using RIPA lysis buffer (Beyotime Biotechnology, P0013C), and protein concentrations were determined using a BCA protein assay kit. Equal amounts of protein samples were separated by 10% SDS-PAGE and electrotransferred onto polyvinylidene fluoride (PVDF) membranes (Millipore, ISEQ00010). The membranes were blocked with 5% non-fat milk at room temperature for 2 h. Subsequently, the membranes were incubated overnight at 4 °C with the following specific primary antibodies: anti-PRDX1 (HUABIO, ET1702-08; 1:1000), anti-TRIM21 (HUABIO, HA721832; 1:1000), anti-TRAF6 (HUABIO, HA722857; 1:1000), anti-GAPDH (HUABIO, ET1601-4; 1:1000), anti-β-actin (HUABIO, HA722023; 1:1000), anti-β-tubulin (HUABIO, ET1602-4; 1:1000), anti-LC3B (HUABIO, ET1701-65; 1:1000), anti-SQSTM1/p62 (HUABIO, HA721171; 1:1000), anti-p65 (ABclonal Technology; 1:10000), anti-phosphorylated (p)-p65 (ABclonal Technology, AP1294; 1:5000), anti-pro-IL-1β (R&D Systems, AF-401-NA; 1:1000),

anti-ubiquitin (HUABIO, ET1609-21; 1:1000), anti-Myc (HUABIO, HA723950; 1:10000), anti-HA (HUABIO, ET1611-49; 1:10000), and anti-FLAG (HUABIO, HA724169; 1:10000). On the following day, the membranes were incubated with the corresponding horseradish peroxidase (HRP)-conjugated secondary antibodies at room temperature for 1.5 h. The protein bands were visualized using a high-sensitivity enhanced chemiluminescence (ECL) kit (Abbkine, BMU102-CN) and captured on a Tanon 5200 Chemiluminescent Imaging System. The densitometric values of the target bands were quantified using ImageJ software (National Institutes of Health, USA).

Quantitative real-time PCR

Total RNA was extracted from the cells using RNA isolator Total RNA Extraction Reagent (Vazyme Biotech Co., Ltd., R401-01). The extracted RNA was subsequently reverse-transcribed into complementary DNA (cDNA) using a First-Strand cDNA Synthesis Kit (Vazyme Biotech Co., Ltd., R021-01). Quantitative real-time PCR (qPCR) amplification was performed using a SYBR Green qPCR Master Mix (Vazyme Biotech Co., Ltd., Q321-02) on a StepOnePlus Real-Time PCR System (Applied Biosystems, USA). The relative mRNA expression levels of the target genes were calculated using the $2^{-\Delta\Delta Ct}$ method, with *β-actin* serving as the internal reference gene for normalization. The specific primer sequences used in this study are detailed in Table S2.

Tissue preparation and immunofluorescence staining

Isolated mouse brain samples were initially fixed in 4% paraformaldehyde (PFA) for 24 h, and subsequently dehydrated in 15% and 30% sucrose solutions at 4 °C for 2 to 3 days until fully equilibrated. Next, the frozen mouse brain tissues were cut into 12-μm-thick coronal sections using a cryostat (Leica, Germany). For immunofluorescence staining, the frozen coronal sections and cell coverslips were post-fixed with 4% PFA and then washed three times with phosphate-buffered saline (PBS, pH 7.4) for 5 min each. Subsequently, the sections or cell coverslips were blocked with PBS containing 10% normal goat serum or alpaca serum at room temperature for 1 h to prevent non-specific binding. The samples were then incubated with specific primary antibodies overnight at 4 °C, followed by incubation with the corresponding secondary antibodies at room temperature for 1 h. Cell nuclei were counterstained with DAPI. Finally, immunofluorescence images were acquired and visualized using an FV3000 confocal laser scanning microscope (Olympus, Japan).

Statistical analysis

Statistical analyses and data visualization were performed using GraphPad Prism software (version 8.0; GraphPad Software, San Diego, CA, USA) and R software (version 4.5.2). All quantitative continuous data are presented as the mean ± standard deviation (SD). For ordinal non-parametric data, such as neurological deficit scores, results are expressed as the median with interquartile range. Prior to conducting parametric tests, data were assessed for normal distribution and homogeneity of variance.

For comparisons between two independent groups, a two-tailed unpaired Student's *t*-test was utilized. For experiments comparing three or more groups with a single independent variable, a one-way analysis of variance (ANOVA) followed by Dunnett's *post hoc* test was performed. For experiments involving two independent variables (e.g., treatment and transfection, or treatment across specific conditions), a two-way ANOVA followed by Sidak's multiple comparisons test was applied. To evaluate continuous data with repeated measures over multiple time points (e.g., long-term behavioral assessments and rotarod tests), a mixed-effects model (REML) was employed, followed by Sidak's or Bonferroni's multiple comparisons test for the main effect of treatment.

Non-parametric tests were strictly employed for ordinal variables; specifically, the Mann-Whitney *U* test was used for two-group comparisons of acute neurological scores, and the Kruskal-Wallis test followed by Dunn's multiple comparisons test was utilized for multiple groups. Survival rates were analyzed using the Kaplan-Meier method, and statistical differences were determined by the Log-rank (Mantel-Cox) test.

For specific kinetic and biophysical calculations, the IC_{50} values were calculated using non-linear regression analysis; differences in thermal degradation curves in the CETSA were analyzed using an extra sum-of-squares F test based on non-linear regression; and the equilibrium dissociation constant (K_D) in SPR was calculated utilizing a steady-state affinity model. Additionally, for single-cell RNA sequencing data, differential gene expression and relevant statistical comparisons were evaluated using the Wilcoxon rank-sum test with Bonferroni correction (adjusted *P* values are shown).

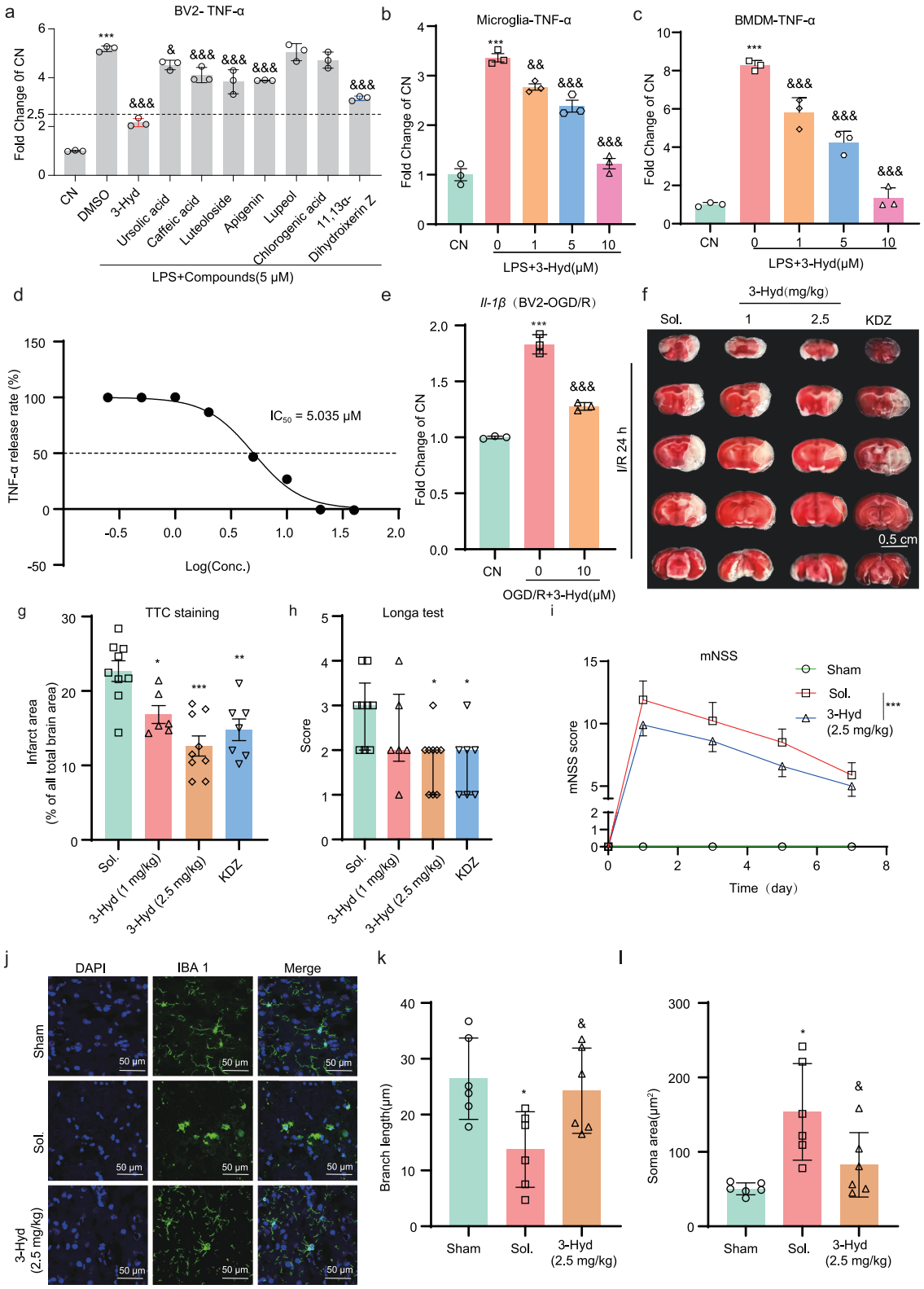
In all biological experiments, "*n*" represents the number of independent biological replicates. A *P*-value of less than 0.05 ($P < 0.05$) was considered to indicate a statistically significant difference.

RESULTS

3-Hydroxydehydroleucodin is the primary component of KDZ that exerts anti-neuroinflammatory effects

To compare the anti-neuroinflammatory effects of KDZ constituents, we employed a two-phase "screening-to-validation" in vitro strategy. In phase 1, a canonical lipopolysaccharide (LPS)-induced inflammation model was used. In terms of an optimal signal-to-noise ratio, the LPS model served as a robust, high-throughput system for initial compound screening and sensitive target fishing. Following the successful identification of the potent efficacy of 3-Hyd and its direct binding targets, phase 2 transitioned exclusively to an oxygen–glucose deprivation/reoxygenation (OGD/R) model. This disease-specific paradigm definitively validated 3-Hyd's core protective mechanisms within an authentic ischemic microenvironment [45]. First, we established a neuroinflammation screening model in a mouse microglial BV2 cell line using LPS stimulation and detected the release levels of the pro-inflammatory cytokine tumor necrosis factor-α (TNF-α) *via* ELISA. We systematically evaluated the anti-inflammatory activities of the main components of KDZ [14, 15], including luteoloside, apigenin, chlorogenic acid, caffeic acid, lupeol, ursolic acid, 3-Hyd, and 11,13α-dihydroixerin Z. The results revealed that at an equimolar concentration (5 μM), compared with that of caffeic acid and luteoloside, 3-Hyd had the best anti-inflammatory effect (Fig. 1a). Consequently, we selected 3-Hyd, which possessed the most anti-inflammatory activity, as the main subject for subsequent mechanistic studies.

We further verified its anti-inflammatory efficacy in primary mouse microglia and found that 3-Hyd (1, 5, and 10 μM) dose-dependently inhibited LPS-induced TNF-α release (Fig. 1b); this potent anti-inflammatory effect was also stable in bone marrow-derived macrophages (BMDMs) (Fig. 1c). Cytotoxicity assays indicated that 3-Hyd at the indicated concentrations did not affect cell viability (Fig. S1a). Furthermore, in BV2 cells, 3-Hyd at 10 μM not only significantly downregulated the mRNA levels of LPS-induced pro-inflammatory cytokines, including *Il-1β*, *Il-6*, and *Tnf-α* (Fig. S1b–d) but also upregulated the expression of the anti-inflammatory cytokine *Il-10* (Fig. S1e). Moreover, the half-maximal inhibitory concentration (IC_{50}) for suppressing TNF-α release was calculated to be approximately 5 μM (Fig. 1d). To mimic the pathological environment of ischemic stroke, we established an OGD/R model in BV2 cells in vitro, and the results confirmed that 3-Hyd could also significantly inhibit the high OGD/R-induced mRNA expression of *Il-1β* (Fig. 1e). Similarly, in the human microglial cell line HMC3, 3-Hyd effectively inhibited the LPS-



induced mRNA expression of various pro-inflammatory cytokines, including *IL-1β*, *IL-6*, and *TNF-α* (Fig. S1f–h), and promoted the transcription of *IL-10* (Fig. S1i).

To evaluate the in vivo cerebroprotective effects of 3-Hyd, we simultaneously administered vehicle or 3-Hyd during the reperfusion phase in a mouse tMCAO model. TTC staining and behavioral evaluation revealed that, compared with the tMCAO + Sol group, 3-Hyd treatment significantly reduced the cerebral infarct area (Fig. 1f, g) and effectively improved the acute-phase neurological deficit score (Fig. 1h), with the protective effect being

Fig. 1 3-Hyd exhibits significant anti-neuroinflammatory effects in vitro and in vivo. a ELISA quantification of TNF-α release in LPS-induced BV2 cells treated with representative monomeric compounds from KDZ ($n = 3$). Dose-dependent inhibition of LPS-induced TNF-α release by 3-Hyd in primary microglia (**b** $n = 3$) and BMDMs (**c** $n = 3$). **d** IC_{50} curve of 3-Hyd inhibiting LPS-induced TNF-α release in BV2 cells, determined via non-linear regression analysis. **e** Inhibitory effect of 3-Hyd on OGD/R-induced *Il-1β* mRNA expression in BV2 cells ($n = 3$). Representative TTC staining images (**f**) and quantitative analysis of cerebral infarct area (**g**) in WT C57BL/6 J male mice 24 h post-tMCAO (60 min). Mice were intravenously injected with saline or 3-Hyd (1, 2.5 mg/kg) or KDZ (4.8 mL/kg) at reperfusion onset ($n = 6$–9/group). **h** Acute-phase neurological deficit scores at 24 h post-reperfusion ($n = 6$–9/group). **i** Modified neurological severity scores were evaluated at 1, 3, 5, and 7 days post-reperfusion ($n = 7$–10/group). Representative morphological images of microglia 24 h post-reperfusion (**j**) with quantitative analysis of microglial branch length (**k**) and soma size (**l**) ($n = 6$/group). Data are presented as mean ± SD. Statistical analyses were performed using one-way ANOVA followed by Dunnett's test (**a–c**, **e**, **g**, **k**, **l**), Kruskal-Wallis test followed by Dunn's multiple comparisons test (**h**) or mixed-effects model (REML) followed by Sidak's multiple comparisons test (**i**). $^{*}P < 0.05$, $^{***}P < 0.001$ vs. CN or tMCAO + Sol group; $^{\&}P < 0.05$, $^{\&\&}P < 0.01$, $^{\&\&\&}P < 0.001$ vs. DMSO, LPS/OGD + 3-Hyd (0 μM), or tMCAO + Sol group.

particularly pronounced in the 2.5 mg/kg high-dose group. Concurrently, KDZ also exhibited substantial neuroprotective effects, which are consistent with previous experimental findings [11, 12]. During the 7-day long-term monitoring of neurological functional recovery, 2.5 mg/kg of 3-Hyd not only significantly increased the postoperative survival rate of tMCAO mice (Fig. S1j) but also resulted in a sustained improvement in multiple motor and sensory function tests. Compared with that in the vehicle group, the performance of mice in the 3-Hyd treatment group was significantly reversed in terms of both the modified neurological severity score (mNSS) (Fig. 1i) and the results of the rotarod test (Fig. S1k) at 1, 3, 5, and 7 days post-reperfusion. We also observed alterations in cell morphology after tMCAO through a series of literature-defined methods for assessing microglial morphological changes [46]. Using these methods, we found that compared with those in the Sham group, microglia in the post-tMCAO group exhibited shortened branch lengths, enlarged soma sizes, and a decreased number of branches (Figs. 1j–l and S1l). These results indicated the differentiation of microglia toward a highly pro-inflammatory state.

Collectively, these in vitro and in vivo data confirmed that 3-Hyd derived from KDZ could potently inhibit neuroinflammatory responses in both mouse and human microglia, significantly alleviate ischemia/reperfusion-induced cerebral infarction in animal models, and promote long-term neurological recovery.

3-Hyd significantly inhibits the activation of the NF-κB signaling pathway and excessive macroautophagy during neuroinflammation

To explore the potential molecular mechanisms underlying the anti-inflammatory effects of 3-Hyd in depth, we established an in vitro inflammation model by stimulating primary bone marrow-derived macrophages (BMDMs) with LPS and performed transcriptome sequencing (RNA-seq) analysis. Compared with immortalized cell lines, primary BMDMs are more physiologically relevant and readily accessible [47], enabling a more authentic reflection of an organism's immune response status. The results of principal component analysis (PCA) revealed that the spatial distribution of the samples from the LPS + 3-Hyd intervention group and the LPS + DMSO model group significantly clustered and separated between groups (Fig. 2a). Analysis of the differentially expressed genes (DEGs) revealed 2847 significant DEGs, including 1375 upregulated genes and 1472 downregulated genes (Fig. 2b, c). The results of the KEGG pathway enrichment analysis of the top 30 pathways revealed that in the Cellular Processes (CellP) category, DEGs were enriched primarily in macroautophagy-related pathways; in the Genetic Information Processing (GenIP) category, they were enriched mainly in protein processing and ubiquitination processes; and in the Environmental Information Processing (EvnIP) and Organismal Systems (OrgaS) categories, they were highly enriched in inflammation-related signaling pathways (Fig. 2d). Furthermore, the enrichment results of the Gene Ontology Biological Process (GO-BP) further confirmed that the downregulated DEGs were significantly enriched in the NF-κB signaling pathway (Fig. S2a), whereas the upregulated DEGs were significantly enriched in ubiquitination signaling pathways (Fig. 2e). These transcriptomic profiles strongly suggested that 3-Hyd might play key regulatory roles in inflammation by intervening in the NF-κB signaling pathway, the macroautophagy network, and protein ubiquitination processes.

To verify the results of the RNA-seq analysis in vitro, we constructed a neuroinflammation model in BV2 microglia using both LPS and OGD/R models. Western blot assays confirmed that in the LPS-induced inflammation model, 3-Hyd significantly inhibited the LPS-induced phosphorylation and activation of p65, the key protein of the NF-κB pathway (Fig. 2f, g), and simultaneously downregulated the expression level of the downstream pro-inflammatory signaling molecule pro-IL-1β (Fig. 2h). Concurrently, 3-Hyd effectively restrained the excessive activation of macroautophagy in BV2 cells under neuroinflammatory stress, which was specifically manifested by the significant inhibition of the aberrantly high expression of the macroautophagy marker LC3B-II (Fig. 2i) and the reversal of the degradation of the protein expression of the macroautophagy substrate SQSTM1/p62 (Fig. 2j). These results were consistently verified in the neuroinflammation model constructed by OGD/R (Fig. 2k–o). Furthermore, to explicitly quantify the impact of 3-Hyd on autophagic flux, we introduced a tandem fluorescent mRFP-GFP-LC3B reporter into BV2 cells. Quantitative puncta analysis revealed that OGD/R exposure induced the massive formation of both autophagosomes (yellow puncta, GFP^{+}/$mCherry^{+}$) and autolysosomes (red puncta, GFP^{-}/$mCherry^{+}$). However, 3-Hyd treatment significantly reduced the absolute numbers of both puncta populations (Fig. S2b, c). These morphological findings, which are consistent with our protein expression data, definitively demonstrate that 3-Hyd effectively suppresses the excessive initiation of microglial autophagy during ischemic injury rather than impairing downstream lysosomal degradation. These findings strongly demonstrated that 3-Hyd effectively suppressed the excessive activation of microglial autophagy during the inflammatory response.

Collectively, the results of the aforementioned multiomics and molecular biology verification demonstrated that the NF-κB cascade and the macroautophagy process co-participate in the pathological progression of neuroinflammation and that 3-Hyd can systematically reverse the neuroinflammatory response through multidimensional targeted regulation of the NF-κB pathway, macroautophagic flux, and potential ubiquitination pathways.

3-Hyd specifically targets the V51 and R128 residues of PRDX1 to exert its anti-neuroinflammatory effects

Small-molecule affinity probe-based pull-down coupled with liquid chromatography–tandem mass spectrometry (pull-down/LC–MS/MS) is a classic chemical biology strategy for identifying the direct intracellular targets of compounds [36, 48]. To identify the direct molecular target through which 3-Hyd (Fig. 3a) exerts anti-neuroinflammatory activity, we synthesized a biotin-labeled

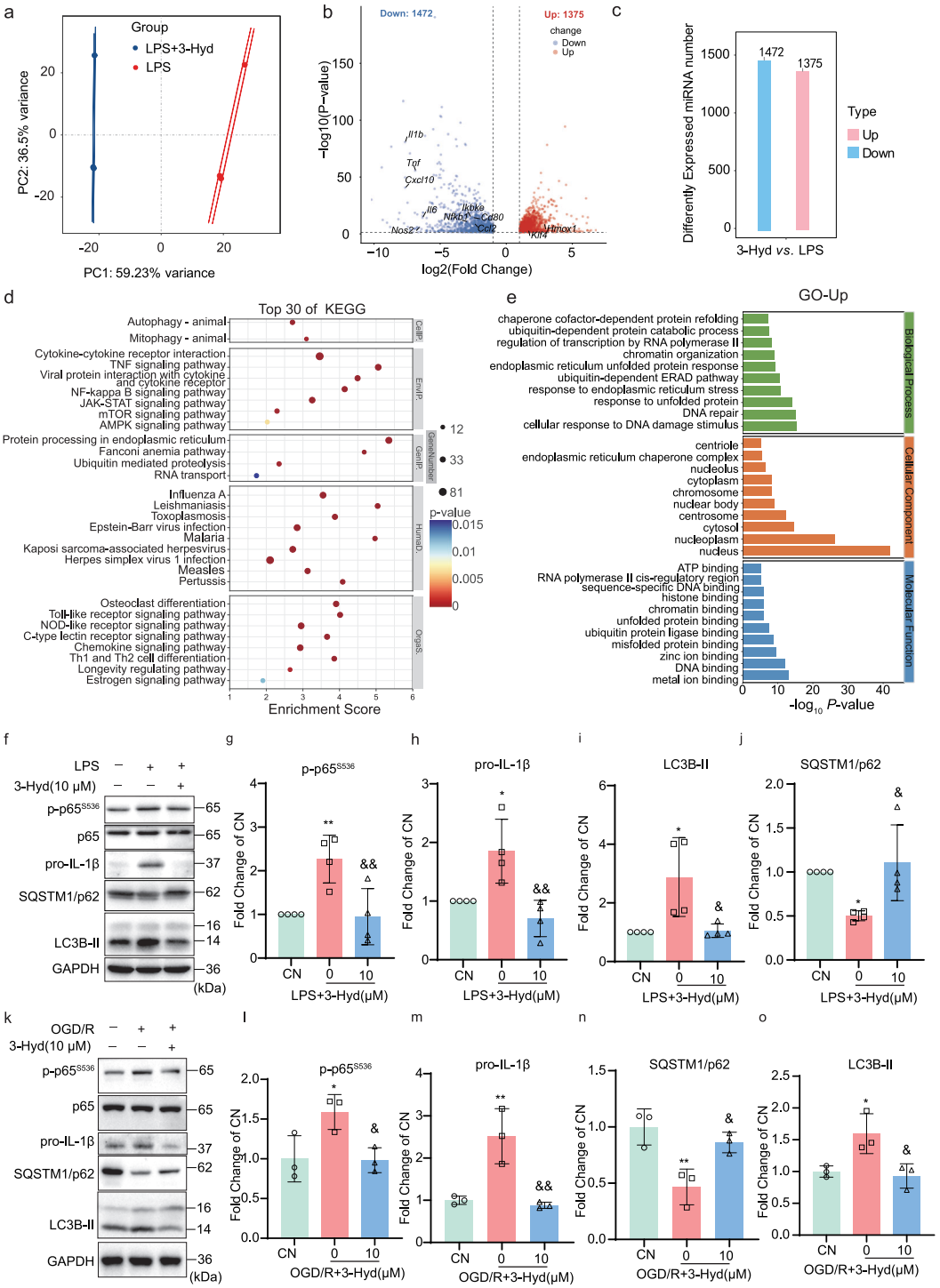


Fig. 2 3-Hyd inhibits NF-κB signaling and excessive autophagy during neuroinflammation. a Principal component analysis (PCA) plot of RNA-seq data from primary BMDMs in the LPS + DMSO and LPS + 3-Hyd groups. Volcano plot (**b**) and bar chart (**c**) of differentially expressed genes (DEGs) in primary BMDMs, displaying 2847 significant DEGs (1375 upregulated, 1472 downregulated). Top 30 enriched KEGG pathways of the DEGs (**d**) and Gene Ontology-Biological Process (GO-BP) enrichment analysis of the upregulated DEGs (**e**). Western blotting evaluation of LPS-induced NF-κB and autophagy pathways in BV2 cells. Representative images (**f**) and quantitative analysis of p-p65^{S536}:p65 (**g**) pro-IL-1β:GAPDH (**h**) LC3B-II:GAPDH (**i**) and SQSTM1/p62:GAPDH (**j**) protein expression ($n = 4$/group). Western blotting evaluation of OGD/R-induced NF-κB and autophagy pathways in BV2 cells. Representative images (**k**) and quantitative analysis of p-p65^{S536}:p65 (**l**) and pro-IL-1β:GAPDH (**m**) and SQSTM1/p62:GAPDH (**n**) and LC3B-II:GAPDH (**o**) protein expression ($n = 3$/group). Data are presented as mean ± SD. Statistical analyses were performed using one-way ANOVA followed by Dunnett's test. *$P < 0.05$, **$P < 0.01$ *vs.* CN group; $^{\&}P < 0.05$, $^{\&\&}P < 0.01$ *vs.* LPS or OGD/R + 3-Hyd (0 μM) group.

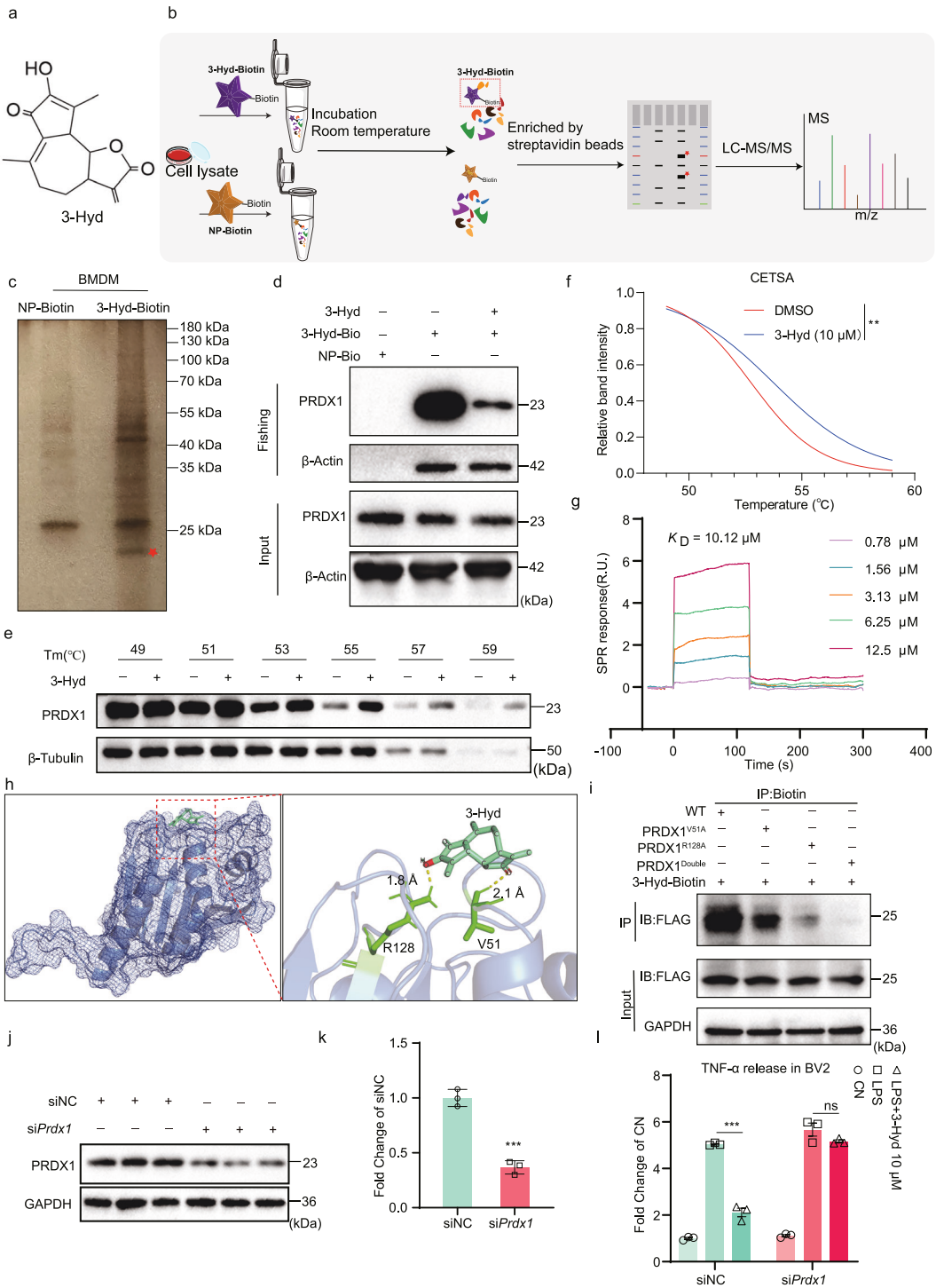


Fig. 3 3-Hyd exerts anti-neuroinflammatory effects by targeting PRDX1 residues V51 and R128. a Chemical structure of 3-Hyd and its biotinylated probe (3-Hyd-Biotin). **b** Schematic workflow of the streptavidin magnetic bead pull-down assay. **c** Silver staining of SDS-PAGE gels showing eluted products from BMDM lysates incubated with NP-Biotin or 3-Hyd-Biotin. **d** Competitive pull-down and Western blotting results showing that free 3-Hyd competitively inhibits 3-Hyd-Biotin binding to PRDX1. Cellular thermal shift assay (CETSA) evaluating the effect of 3-Hyd on PRDX1 thermal stability. Representative Western blotting images across a temperature gradient (**e**) and relative quantification curve of PRDX1 thermal degradation (**f**). **g** Surface plasmon resonance (SPR) measurement of binding kinetics between 3-Hyd and recombinant human PRDX1 (K_D = 10.12 μM, calculated via steady-state affinity model). **h** Molecular docking model of 3-Hyd in the PRDX1 binding pocket (PDB ID: 4XCS), displaying the hydrogen bond network with V51 and R128. **i** Pull-down and Western blotting verification of 3-Hyd-Biotin binding capacity with wild-type (WT), single mutant ($PRDX1^{V51A}$, $PRDX1^{R128A}$), and double mutant ($PRDX1^{V51A\&R128A}$) proteins. Reversal experiment verifying the efficacy of 3-Hyd following siRNA-mediated knockdown of Prdx1 in BV2 cells. Western blotting (**j**) and statistical analysis (**k**) of Prdx1 knockdown efficiency. **l** Inhibitory effect of 3-Hyd on LPS-induced TNF-α release after Prdx1 knockdown. Data are presented as mean ± SD (n = 3/group). Statistical analyses were performed using extra sum-of-squares F test based on non-linear regression (**f**) unpaired Student's t-test (**k**) or two-way ANOVA followed by Sidak's multiple comparisons test (**l**). $^{**}P < 0.01$ *vs*. overall Veh. group; $^{***}P < 0.001$ *vs*. siNC group; n.s. (not significant), $^{***}P < 0.001$ *vs*. LPS group within the same transfection group.

probe of 3-Hyd, designated 3-Hyd-Biotin (Fig. S3a). We collected BMDM whole-cell lysates and incubated them with either a negative control probe (NP-Biotin) or 3-Hyd-Biotin and subsequently enriched potential binding proteins using streptavidin magnetic beads (Fig. 3b). Gel electrophoresis and silver staining analysis of the eluted products revealed that compared with the NP-Biotin control group, the 3-Hyd-Biotin group exhibited specifically enriched protein bands at molecular weights of approximately 23 and 42 kDa (Fig. 3c). These differential bands were excised and subjected to mass spectrometry for protein identification. By cross-referencing these results with the pathway enrichment profiles revealed by our preceding RNA-seq analysis, we identified peroxiredoxin 1 (PRDX1) as a candidate target protein that is concurrently involved in the regulation of both the NF-κB and macroautophagy pathways [49]. Subsequent competitive pull-down and immunoblotting assays in BMDMs revealed that 3-Hyd-Biotin specifically enriched the PRDX1 protein, and this binding was significantly inhibited by the addition of free 3-Hyd (Fig. 3d). Conversely, β-actin, which was abundant at the 42 kDa position, could not be competitively inhibited by free 3-Hyd (Fig. 3d). This directly targeted interaction was robustly reproduced in primary microglia (Fig. S3b) and in the mouse microglial BV2 cell line (Fig. S3c). Therefore, in subsequent mechanistic investigations, we consistently utilized BV2 cells in the in vitro model.

Furthermore, the cellular thermal shift assay (CETSA) provided additional physiological evidence for this target engagement [50]. The binding of 3-Hyd significantly increased the conformational thermal stability of the PRDX1 protein; particularly under high-temperature challenge at 55 °C, 3-Hyd effectively delayed the heat-induced denaturation and degradation of PRDX1 (Fig. 3e, f). Surface plasmon resonance (SPR) is the gold standard for real-time, label-free evaluation of the binding affinity and kinetics between small molecules and target proteins [51]. SPR analysis revealed that the binding between 3-Hyd and recombinant human PRDX1 exhibited "fast-on, fast-off" kinetics, with an equilibrium dissociation constant (K_D) of approximately 10.12 μM (Fig. 3g), suggesting that their interaction was primarily reversible and noncovalent.

Given that the chemical structure of 3-Hyd contains an α,β-unsaturated carbonyl moiety, which potentially reacts to form covalent bonds with surface cysteine (Cys) residues on proteins [52, 53], we constructed four key cysteine-mutant plasmids of *Prdx1*: PRDX1^{C52A}, PRDX1^{C71A}, PRDX1^{C83A}, and PRDX1^{C173A}. However, pull-down validation indicated that even when these potential covalent binding sites were mutated, 3-Hyd-Biotin could still effectively bind to the aforementioned mutant PRDX1 proteins (Fig. S3d). Combined with the SPR data, these findings strongly confirmed that the binding between 3-Hyd and PRDX1 was noncovalent. The cross-validation results from these multi-dimensional techniques conclusively established that PRDX1 is the direct target protein of 3-Hyd.

To precisely map the noncovalent binding pocket of 3-Hyd on PRDX1, we performed molecular docking simulations using AutoDock [42]. The docking model predicted that 3-Hyd could form a stable hydrogen bond network with the V51 and R128 residues of PRDX1 (PDB ID: 4XCS). Specifically, it formed a hydrogen bond with the V51 residue (at a distance of 2.1 Å) and another hydrogen bond with the R128 residue (at a distance of 1.8 Å), contributing to a binding free energy of −7.06 kcal/mol (Fig. 3h). To experimentally verify this structural biology prediction, we constructed expression vectors for wild-type (WT) PRDX1, single-point mutants (PRDX1^{V51A} and PRDX1^{R128A}), and a double-point mutant (PRDX1$^{V51A/R128A}$) and transfected them into HEK293T cells for interaction assessment. Compared with WT PRDX1, the single mutation of either V51 or R128 only partially attenuated the target enrichment capability of 3-Hyd-Biotin. Strikingly, when both V51 and R128 were simultaneously mutated, the binding of 3-Hyd to PRDX1-FLAG was almost entirely abolished (Fig. 3i). These results confirmed that V51 and R128 were the critical amino acid sites mediating the binding of 3-Hyd to PRDX1.

Finally, to verify whether the anti-neuroinflammatory effects of 3-Hyd depended specifically on its targeted binding to PRDX1, we knocked down the endogenous expression of PRDX1 in BV2 cells using siRNA. Pharmacological reversal experiments demonstrated that, compared with the siNC control, knockdown of PRDX1 significantly abolished the inhibitory effect of 3-Hyd on LPS-induced TNF-α release (Fig. 3j–l). Furthermore, in a PRDX1 knockdown background, the suppressive effects of 3-Hyd on NF-κB signaling activation and excessive macroautophagic flux were markedly blunted (Fig. S3e–h). To evaluate the target selectivity of 3-Hyd, we analyzed the sequence of PRDX2, the closest homolog that shares 77.8% sequence identity with that of PRDX1 (Fig. S3i). Structural comparisons revealed that despite having conserved interacting residues, the 3D pocket of PRDX2 exhibits geometric distortion and conformational incompatibility, preventing stable 3-Hyd accommodation (Fig. S3j). This prediction was empirically confirmed by a pull-down assay, in which 3-Hyd-Bio completely failed to interact with overexpressed PRDX2-FLAG (Fig. S3k). Although we have previously demonstrated that 3-Hyd does not covalently bind to PRDX1, whether noncovalent interactions might still compromise its intrinsic peroxidase activity remains unclear. To address this, we performed an in vitro enzymatic activity assay. The results revealed that at concentrations of up to 10 μM, 3-Hyd had a negligible inhibitory effect on PRDX1 peroxidase activity (Fig. S3l). Collectively, these results demonstrated that 3-Hyd specifically exerted its anti-neuroinflammatory activity by noncovalently binding to the V51 and R128 dual amino acid sites of PRDX1.

3-Hyd targets PRDX1 in microglia to improve cerebral infarction and neurological functional recovery in mice

On the basis of the results of the aforementioned in vitro experiments confirming that 3-Hyd could potently inhibit neuroinflammation by targeting PRDX1, we further investigated whether the cerebroprotective effects of 3-Hyd specifically depended on PRDX1 in microglia at the whole animal level. To this end, we established a microglia-specific conditional inducible knockdown model using *Cx3cr1*$^{Cre/ERT2}$ transgenic mice (Fig. S4a). Specific adeno-associated viruses carrying short hairpin RNA (pAAV-CMV-ZsGreen1-U6-DIO-sh*Prdx1* or the control virus pAAV-CMV-ZsGreen1-U6-DIO-shNC) were microinjected into the right cerebral cortex of the mice via stereotaxic technology. Fourteen days later, tamoxifen was intraperitoneally injected for 5 consecutive days to induce Cre recombinase expression and achieve gene-specific knockdown in microglia. Seven days after the final administration, tMCAO surgery was performed to construct the ischemia-reperfusion model (Fig. 4a).

Evaluation of viral transduction efficiency revealed that the ZsGreen1 fluorescent signal carried by the AAV precisely co-localized with microglia in the brain (Fig. 4b). Immunofluorescence (IF) staining further confirmed that compared with that in the control group injected with the shNC virus, the protein expression level of PRDX1 in microglia was significantly and specifically downregulated in mice injected with the sh*Prdx1* virus in the cerebral cortex (Fig. S4b, c).

With respect to functional phenotype assessment, 2,3,5-triphenyltetrazolium chloride (TTC) staining revealed that, compared with shNC *Cx3cr1*$^{Cre/ERT2}$ mice, microglia-specific knockdown of *Prdx1* (the sh*Prdx1* group) exacerbated the cerebral infarct volume to some extent, although the difference did not reach statistical significance (Fig. 4c, d). This trend is consistent with effects previously observed in *Prdx1* global knockout mice [23]. Crucially, in shNC control mice, 3-Hyd treatment significantly reduced cerebral infarction and improved Longa scores; however,

following microglia-specific knockdown of PRDX1 (the sh*Prdx1* group), these cerebroprotective effects of 3-Hyd were completely abolished (Fig. 4c–e).

Furthermore, monitoring of long-term neurological functional recovery (up to 7 days) revealed that in the shNC background, 3-Hyd significantly increased the postoperative survival rate of tMCAO mice (Fig. 4f) and significantly promoted recovery, as indicated by both the modified neurological severity score (mNSS) (Fig. 4g) and the results of the rotarod test (Fig. 4h). Similarly, when PRDX1 was specifically knocked down in microglia, the beneficial effects of 3-Hyd on these long-term prognostic indicators were significantly attenuated (Fig. 4f–h), indicating that the cerebroprotective effects of 3-Hyd in vivo were mediated mainly by its targeting protein, namely, PRDX1, in microglia.

3-Hyd stabilizes the PRDX1 protein pool by preventing its ubiquitin-proteasome degradation

Building upon the discovery that 3-Hyd targets PRDX1 to exert anti-neuroinflammatory effects, we further investigated the specific molecular mechanisms underlying its regulation of PRDX1. First, we comprehensively evaluated the effects of 3-Hyd on PRDX1 at both the transcriptional (mRNA) and translational (protein) levels. RT–qPCR results revealed that LPS stimulation of BV2 cells for 6 h did not cause significant changes in the *Prdx1* mRNA level and that 3-Hyd treatment similarly did not affect the transcription of *Prdx1* (Fig. 5a). However, Western blot analysis revealed that the protein expression level of PRDX1 was significantly decreased after 6 h of LPS stimulation, whereas 10 μM 3-Hyd effectively suppressed the LPS-induced degradation of the PRDX1 protein (Fig. 5b, c).

Therefore, we established a concentration gradient of 3-Hyd (1, 5, and 10 μM, with a fixed 6 h of LPS stimulation) and a time course of LPS stimulation (1, 3, 6, and 9 h, with a fixed 3-Hyd concentration) to thoroughly evaluate the protective effect of 3-Hyd on PRDX1 protein stability. Concentration gradient experiments confirmed that the ability of 3-Hyd to inhibit PRDX1 degradation was significantly dose-dependent (Fig. 5d, e). The results of time-course experiments revealed that the degradation program of the PRDX1 protein began after 3 h of LPS stimulation and progressively decreased over time; 3-Hyd treatment significantly prevented this dynamic degradation process, with the protective effect being particularly prominent at the 6 and 9 h time points of LPS stimulation (Fig. 5f, g). Immunofluorescence staining experiments also confirmed this conclusion; 3-Hyd significantly reversed the attenuation of the mean fluorescence intensity of the PRDX1 protein caused by LPS stimulation (Fig. 5h, i).

Intracellular protein degradation is a highly orchestrated process that primarily relies on the ubiquitin–proteasome system (UPS) and the macroautophagy–lysosome pathway [54]. To clarify the specific degradation pathway of the PRDX1 protein, we used the protein synthesis inhibitor cycloheximide (CHX), the proteasome-specific inhibitor MG132, and the lysosomal inhibitor hydroxychloroquine (HCQ) in combination with 3-Hyd in an LPS-induced inflammation model. The results revealed that the administration of MG132 alone significantly blocked the LPS-induced degradation of the PRDX1 protein, and its rescue effect was highly similar to that of 3-Hyd (Fig. 5j, k). These findings strongly suggest that the degradation of PRDX1 is dependent mainly on the proteasome pathway and that 3-Hyd most likely maintains the stability of PRDX1 by intervening in this pathway.

To confirm this hypothesis, we directly evaluated the regulatory effect of 3-Hyd on the global ubiquitination level of PRDX1 in BV2 cells. Immunoprecipitation and ubiquitination assays confirmed that 3-Hyd significantly decreased the degree of ubiquitination of the PRDX1 protein under LPS stress conditions (Fig. 5l). Collectively, these results demonstrated that during the pathological progression of neuroinflammation, the degradation of the PRDX1 protein accelerated *via* the ubiquitin–proteasome system, whereas 3-Hyd successfully stabilized and protected the PRDX1 protein pool by inhibiting this ubiquitination–degradation cascade, thus exerting neuroprotective effects.

3-Hyd suppresses neuroinflammation by inhibiting the TRIM21-mediated ubiquitination of PRDX1 at the K109 residue

The ubiquitin–proteasome system is a highly specific protein degradation network in eukaryotic cells that guides target proteins to the proteasome for degradation by covalently attaching ubiquitin tags [55]. During this process, E3 ubiquitin ligases are responsible for specifically recognizing substrates and catalyzing the covalent attachment of ubiquitin molecules to specific lysine (K) residues on the target protein, which is the core rate-limiting step determining ubiquitination specificity [56]. Therefore, identifying the specific ubiquitination site of PRDX1 is crucial for elucidating the targeted anti-inflammatory mechanism of 3-Hyd. There are 19 lysine residues in the sequence of the human PRDX1 protein. Using site-directed mutagenesis, we individually mutated these 19 lysine residues to arginine (R) and co-transfected them with a ubiquitin-MYC expression plasmid into HEK293T cells. Co-immunoprecipitation (Co-IP) revealed that when the 109th lysine residue was mutated (K109R), the global ubiquitination level of PRDX1 significantly decreased (Fig. 6a), indicating that K109 was the key receptor site for the ubiquitination of PRDX1. Multiple sequence alignment of the amino acid sequence of PRDX1 was performed for six representative species (*Homo sapiens*, *Mus musculus*, *Rattus norvegicus*, *Macaca mulatta*, *Gallus gallus*, and *Canis lupus familiaris*). The alignment demonstrates that the lysine 109 (K109) residue, indicated by the black arrowhead and highlighted in red, is strictly conserved among these species, underscoring its fundamental role as a critical ubiquitination site (Fig. 6b). To further verify the biological function of K109 ubiquitination in neuroinflammation, we transfected the PRDX1^{K109R} mutant plasmid into BV2 microglia. The results demonstrated that this mutant also significantly enhanced the inhibitory effect on the activation of core indicators of the NF-κB and macroautophagy pathways (p-p65, pro-IL-1β, SQSTM1/p62, and LC3B-II) (Figs. 6c and S5a–d). Moreover, in the overexpression system, the ubiquitination level of the PRDX1^{K109R} mutant itself was significantly lower than that of WT PRDX1 (Fig. S5e).

As an exquisite post-translational modification, the molecular fate mediated by protein ubiquitination largely depends on the number of ubiquitin molecules polymerizing and the linkage topology of the ubiquitin chain, which act like different instruction tags attached to proteins [57]. Polyubiquitination has the most diverse functions, primarily including linkage types such as K11, K48, and K63 [58]. To determine the specific ubiquitination type of PRDX1, we constructed K11, K48, and K63 single-site mutants of ubiquitin. Co-IP assays confirmed that when the K48 site of ubiquitin was mutated, the polyubiquitination level of PRDX1 decreased (Fig. 6d), confirming that PRDX1 predominantly underwent K48-linked ubiquitin-dependent degradation.

As specific determinants in the UPS [59], E3 ubiquitin ligases are responsible for precisely recognizing target proteins and catalyzing ubiquitin transfer. To identify the upstream E3 ligase that catalyzes PRDX1 ubiquitination, we enriched protein complexes that interact with PRDX1 *via* Co-IP and subjected them to liquid chromatography–tandem mass spectrometry (LC–MS/MS) identification. Statistical analysis of the mass spectrometry data (retaining only candidate proteins with >1 identified peptide) revealed that TRIM21 (identified with 16 specific peptides) and TRIM33 (8 peptides) were the top two candidate E3 ligases, whereas MKRN1 was identified with only 4 peptides (Fig. S5f). All proteins identified by the 3-Hyd-Biotin pull-down/LC-MS/MS assay are detailed in Supplementary Table 1. Subsequent Co-IP validation experiments confirmed that PRDX1 strongly and specifically physically interacted with TRIM21, whereas TRIM33

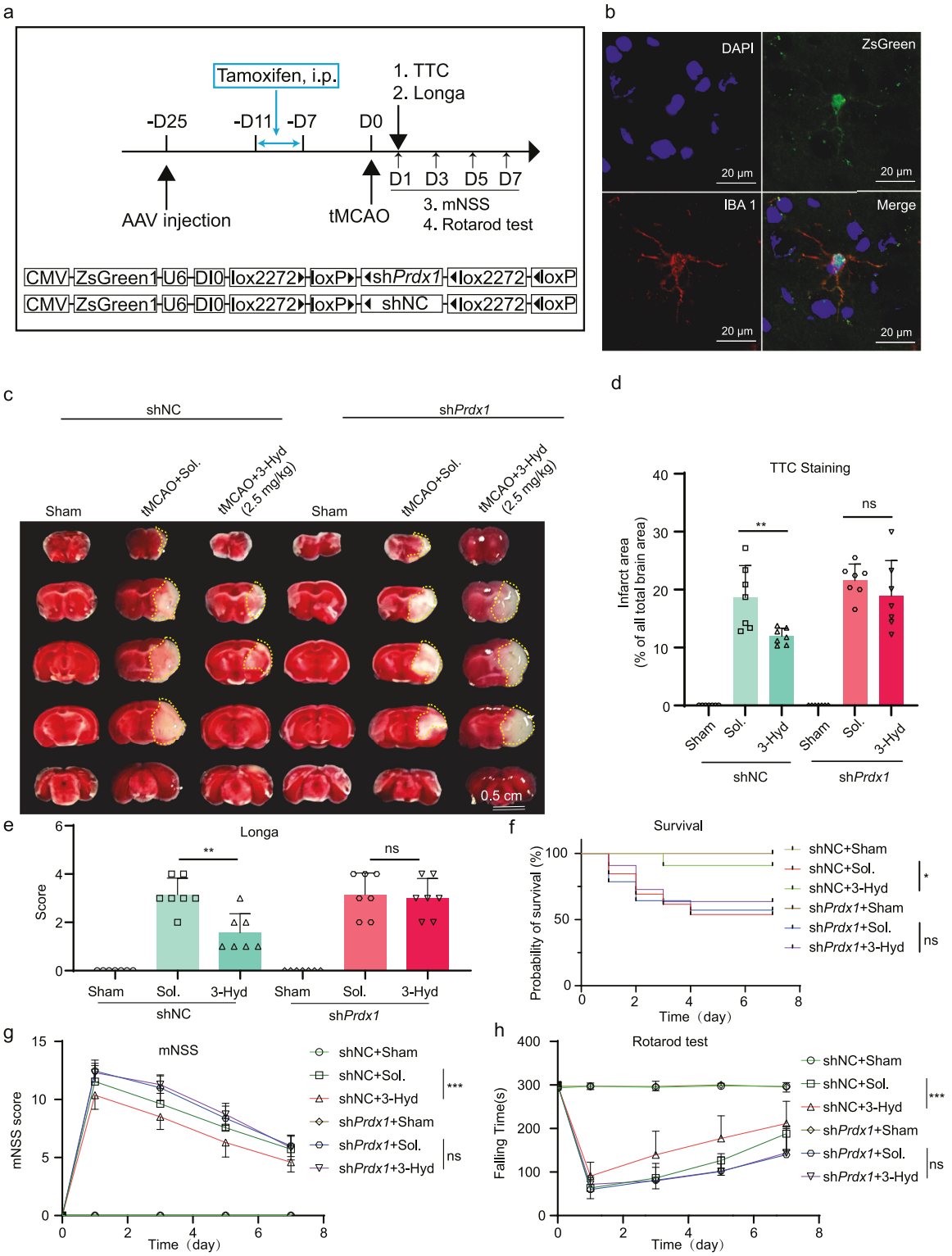


Fig. 4 3-Hyd targets microglial PRDX1 to reduce infarct area and improve neurological function. a Experimental timeline for microglia-specific *Prdx1* knockdown (using *Cx3cr1*$^{Cre/ERT2}$ mice), tMCAO surgery, and 3-Hyd administration. **b** Representative immunofluorescence images confirming the colocalization of AAV-carried ZsGreen1 with microglial markers in the cerebral cortex 14 days post-injection. Representative TTC staining images (**c**) and quantitative analysis of cerebral infarct area (**d**) at 24 h post-reperfusion. **e** Longa neurological deficit scores evaluated at 24 h post-reperfusion. Long-term evaluation of specific microglial *Prdx1* knockdown on the neuroprotective role of 3-Hyd over 7 days via survival curves (**f**) modified neurological severity scores (mNSS) (**g**) and rotarod test (**h**). Data are presented as mean ± SD ($n = 7$–10/group), except for (**e**) which is presented as median with interquartile range ($n = 7$/group). Statistical analyses were performed using two-way ANOVA (**d**), Kruskal-Wallis test (**e**), Log-rank (Mantel-Cox) test (**f**), or mixed-effects model (REML) (**g**, **h**) followed by Sidak's or Dunn's multiple comparisons test. $^{*}P < 0.05$, $^{**}P < 0.01$, $^{***}P < 0.001$ *vs.* shNC + tMCAO + Sol group; n.s. (not significant) vs. sh*Prdx1* + tMCAO + Sol group.

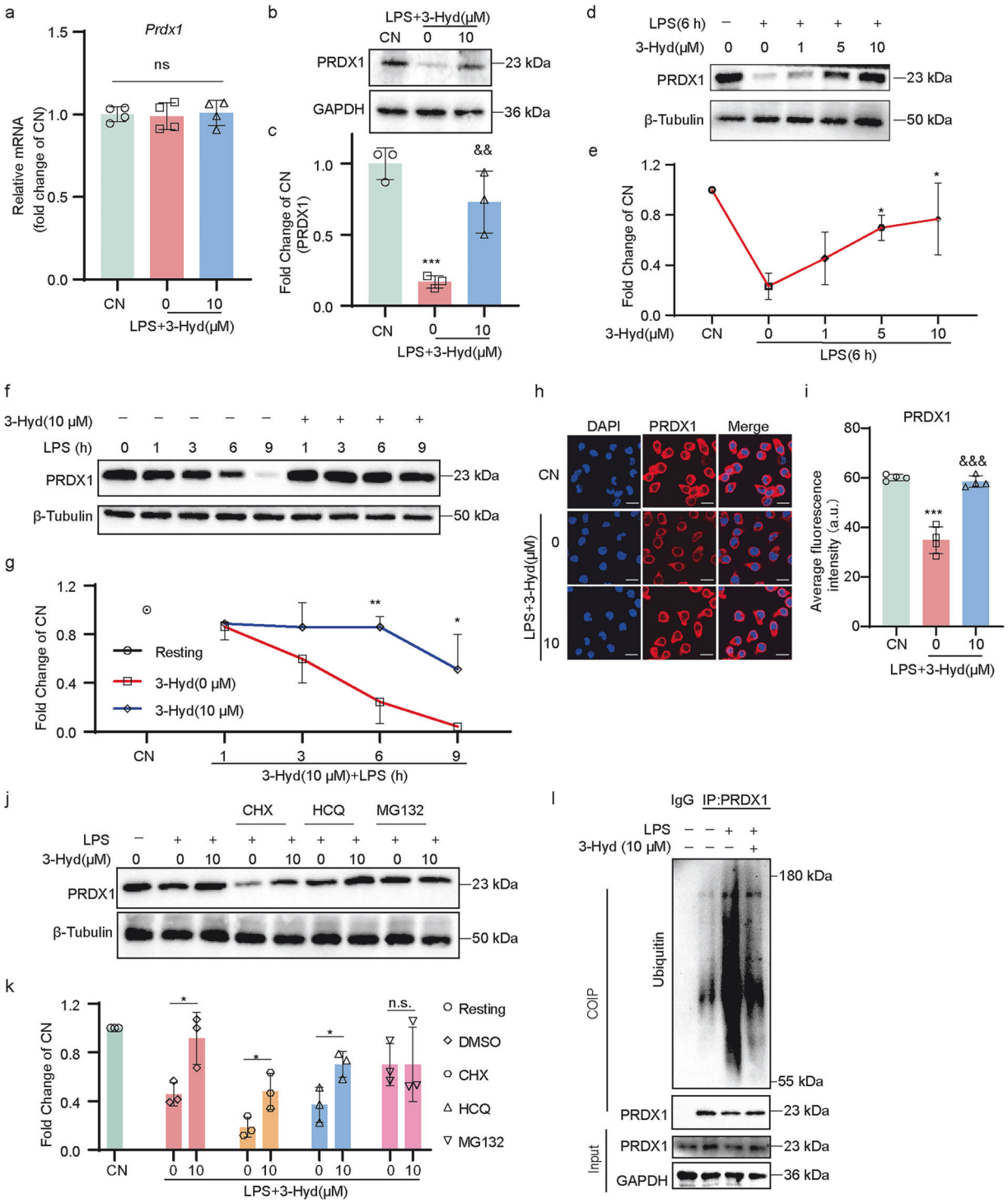
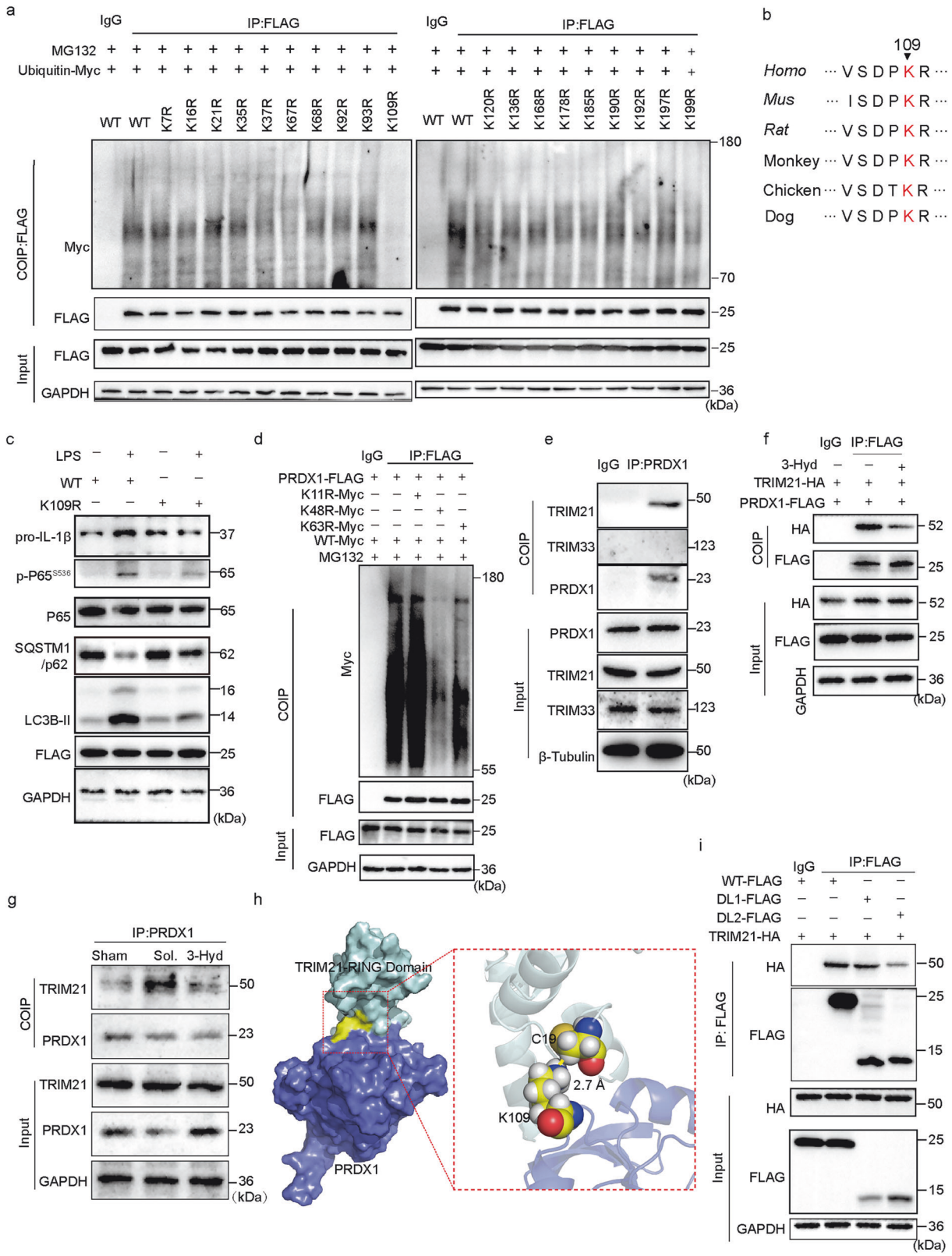


Fig. 5 3-Hyd inhibits PRDX1 degradation *via* the ubiquitin-proteasome pathway. a RT-qPCR analysis of *Prdx1* mRNA levels in BV2 cells after 6 h of LPS stimulation with or without 3-Hyd treatment ($n = 4$). Western blotting evaluation of PRDX1 protein levels. Representative images (**b**) and quantification (**c**) after 6 h of LPS induction ($n = 3$). Representative images (**d**) and quantification (**e**) showing the concentration-dependent (1, 5, 10 μM) protective effect of 3-Hyd against LPS-induced degradation ($n = 3$). Time-course evaluation (1, 3, 6, 9 h) of 3-Hyd on PRDX1 protein stability under LPS stimulation. Representative images (**f**) and quantification (**g**) ($n = 4$). Immunofluorescence staining of PRDX1 expression and distribution in BV2 cells. Representative images (**h** scale bar = 20 μm) and quantitative mean fluorescence intensity (MFI) (**i** $n = 4$). Western blotting evaluating the effects of a protein synthesis inhibitor (CHX), proteasome inhibitor (MG132), and lysosome inhibitor (HCQ) on PRDX1 degradation 3 h post-LPS induction. Representative images (**j**) and quantification (**k** $n = 3$). **l** Representative immunoprecipitation (IP) and Western blotting images detecting overall PRDX1 ubiquitination levels in BV2 cells under LPS incubation. Data are presented as mean ± SD. Statistical analyses were performed using one-way ANOVA followed by Dunnett's test (**a**, **c**, **e**, **i**) or two-way ANOVA followed by Sidak's multiple comparisons test (**g**, **k**). $^{*}P < 0.05$, $^{**}P < 0.01$, $^{***}P < 0.001$ *vs.* CN, LPS + DMSO (at the same time point), or LPS + 3-Hyd (0 μM) group; $^{\&\&}P < 0.01$, $^{\&\&\&}P < 0.001$ *vs.* LPS + 3-Hyd (0 μM) group; n.s. (not significant).



was not enriched (Fig. 6e). In vitro overexpression assays further demonstrated that TRIM21 could significantly upregulate the global ubiquitination level of PRDX1 (Fig. S5g). Importantly, in the overexpression system, 3-Hyd treatment significantly disrupted the interaction between PRDX1 and TRIM21 (Fig. 6f). Next, we evaluated the interaction between PRDX1 and TRIM21 under LPS conditions in BV2 cells. The results indicated that LPS significantly increased the interaction between TRIM21 and PRDX1, whereas

Fig. 6 3-Hyd inhibits neuroinflammation by preventing TRIM21-mediated ubiquitination of PRDX1 at the K109 residue. a Representative Western blotting images of PRDX1 ubiquitination following co-transfection of WT PRDX1 or specific lysine mutants with Ubiquitin plasmids in HEK293T cells. **b** Evolutionary conservation of the Lys109 (K109) residue in PRDX1 across diverse species. Representative Western blotting images showing the effects of WT PRDX1 or PRDX1^{K109R} mutant transfection on NF-κB and autophagy pathway proteins in LPS-induced BV2 cells (**c**) and determining the PRDX1 polyubiquitination linkage type after co-transfection with distinct Ubiquitin linkage mutants (K11R, K48R, K63R) in HEK293T cells (**d**). Representative Co-IP and Western blotting images verifying the specific interactions between PRDX1 and candidate E3 ubiquitin ligases (TRIM21 and TRIM33) (**e**) evaluating the disruptive effect of 3-Hyd on the PRDX1-TRIM21 interaction in an overexpression system (**f**) and analyzing their pathological interaction in microglia sorted from ischemic brain tissues of tMCAO mice following 3-Hyd administration (**g**). **h** 3D protein-protein interaction (PPI) docking model of the TRIM21 RING domain (PDB: 6FGA) and PRDX1 (PDB: 4XCS), demonstrating extreme spatial proximity between the TRIM21 catalytic site (Cys19) and the PRDX1 ubiquitination receptor site (K109). **i** Co-IP assays mapping the TRIM21-interaction region using full-length PRDX1 (WT, AA 1–199) and its truncations (DL1: AA 106–199; DL2: AA 1–105).

3-Hyd decreased this interaction (Fig. S5h). We subsequently validated these findings in BV2 cells subjected to OGD/R. The results revealed that OGD/R injury robustly enhanced the endogenous interaction between PRDX1 and TRIM21 while concurrently increasing the polyubiquitination level of PRDX1; strikingly, these pathological alterations were significantly abrogated by 3-Hyd treatment (Fig. S5i). We subsequently reproduced this mechanism in a mouse tMCAO in vivo model. Compared with that in the Sham group, the binding between PRDX1 and TRIM21 in microglia from brain tissues was significantly greater in the ischemia–reperfusion group; however, 3-Hyd administration effectively reversed these pathological interactions (Fig. 6g). Concurrently, we investigated the inflammatory status and macroautophagy activation in microglia during ischemia–reperfusion. The results suggested that at 24 h post-reperfusion, the phosphorylation levels of pro-IL-1β and p65 were significantly increased. Moreover, the expression of the macroautophagy marker SQSTM1/p62 was significantly downregulated, and that of LC3B-II was significantly upregulated, which was accompanied by a marked decrease in the level of the PRDX1 protein; conversely, 3-Hyd treatment significantly reversed these protein alterations (Fig. S5j–o). These data demonstrated that 3-Hyd inhibited the ubiquitination and degradation of PRDX1 by blocking its binding with TRIM21.

The RING domain within the TRIM21 structure is the core region where it performs its E3 ubiquitin ligase catalytic activity [60]. We performed protein–protein docking (PPI) simulation calculations between the RING domain of TRIM21 (PDB: 6FGA) and that of PRDX1 (PDB: 4XCS) using the HADDOCK v2.4 platform. A structural docking model revealed that the cysteine residue (Cys19) [61] in the catalytic active center of TRIM21 was extremely adjacent to the ubiquitination target site (K109) of PRDX1 in three-dimensional space, with a distance of only 2.7 Å, indicating excellent catalytic accessibility (Fig. 6h). To map the specific interaction interface, we constructed expression plasmids for full-length PRDX1 (WT, AA 1-199) and two truncated mutants: DL1 (AA 106-199) and DL2 (AA 1-105). Co-transfection assays confirmed that when the N-terminal AA 1-105 sequence of PRDX1 was deleted (i.e., overexpressing DL1, retaining AA 106-199), its binding capacity to TRIM21 was maintained; however, when the AA 106-199 region was deleted, the interaction was significantly weakened (Fig. 6i). These findings suggested that TRIM21 is primarily anchored to the AA 106-199 region of PRDX1, where the critical ubiquitination receptor K109 is precisely located.

Collectively, these results confirmed that 3-Hyd could specifically intervene in the interaction between the E3 ubiquitin ligase TRIM21 and PRDX1, thus blocking the K48-linked polyubiquitination and degradation of PRDX1 at the K109 residue, which may be responsible for its anti-neuroinflammatory activity.

3-Hyd attenuates neuroinflammation through the PRDX1-TRAF6 axis

PRDX1 can interact with the RING finger domain of TRAF6 to inhibit its ubiquitination and ligase activity, thus negatively regulating the inflammatory cascade induced by TLR4 stimulation [49]. This classic crosstalk between ubiquitination and the NF-κB signaling pathway was highly consistent with our previous observations from the RNA-seq enrichment analysis (Fig. 2d). Therefore, to further explore the specific downstream molecular mechanisms through which 3-Hyd blocks neuroinflammation after targeting PRDX1, we evaluated the effect of 3-Hyd on the ubiquitination status of TRAF6 using co-immunoprecipitation (Co-IP) assays in a BV2 microglial model. The results clearly demonstrated that 3-Hyd treatment significantly inhibited the global ubiquitination level of TRAF6 (Fig. 7a).

To functionally verify whether the anti-neuroinflammatory effect of 3-Hyd specifically depended on downstream TRAF6, we knocked down endogenous TRAF6 in BV2 cells using siRNA technology and detected the release level of the pro-inflammatory cytokine TNF-α *via* ELISA. Compared with that in the siNC + 3-Hyd control group, the original potent anti-inflammatory effect of 3-Hyd was significantly abolished in the TRAF6 knockdown group (Figs. 7b, c and S6a). Furthermore, knocking down TRAF6 alone effectively inhibited LPS-induced TNF-α release (Fig. 7c), which was consistent with the findings of previous studies reporting that overexpressing TRAF6 promotes the occurrence of neuroinflammation [62].

To further confirm that 3-Hyd inhibits TRAF6 ubiquitination by binding to PRDX1, we overexpressed plasmids for wild-type (WT) PRDX1 and a double mutant lacking 3-Hyd binding capacity (PRDX1$^{V51A/R128A}$) in BV2 cells. Co-IP assays revealed that under WT PRDX1 overexpression conditions, 3-Hyd potently inhibited the ubiquitination of TRAF6; however, when the 51st and 128th amino acids of PRDX1 were mutated to alanine, the inhibitory effect of 3-Hyd on TRAF6 ubiquitination was significantly abolished (Fig. 7d). In parallel with the results of the cellular phenotype experiments, compared with the empty vector group, the group in which WT PRDX1 was overexpressed exhibited significantly inhibition of LPS-induced TNF-α release, and combined 3-Hyd treatment resulted in a stronger synergistic inhibitory effect. Similarly, in the PRDX1 double-mutant background, this pharmacological inhibitory effect was completely abolished (Figs. 7e, f and S6b).

Finally, to explore how the ubiquitination and degradation of PRDX1 reversely affect the ubiquitination status of TRAF6, we overexpressed WT PRDX1 or its ubiquitination-resistant mutant (PRDX1^{K109R}) in BV2 cells. Co-IP revealed that in WT-overexpressing cells, LPS stimulation significantly promoted the ubiquitination of TRAF6; however, when the PRDX1^{K109R} mutation was introduced—which blocked the degradation of PRDX1 itself—LPS-induced TRAF6 ubiquitination was strongly inhibited (Fig. 7g). At the inflammatory phenotype level, overexpressing WT PRDX1 significantly inhibited TNF-α release under LPS conditions, and combined treatment with 3-Hyd further amplified this inhibitory effect; the anti-inflammatory effect of the PRDX1^{K109R} mutation further increased, while combined treatment with 3-Hyd had no additive effects (Figs. 7h, i and S6c). Collectively, by specifically targeting and stabilizing PRDX1, 3-Hyd effectively inhibited the neuroinflammatory cascade mediated by TRAF6 ubiquitination.

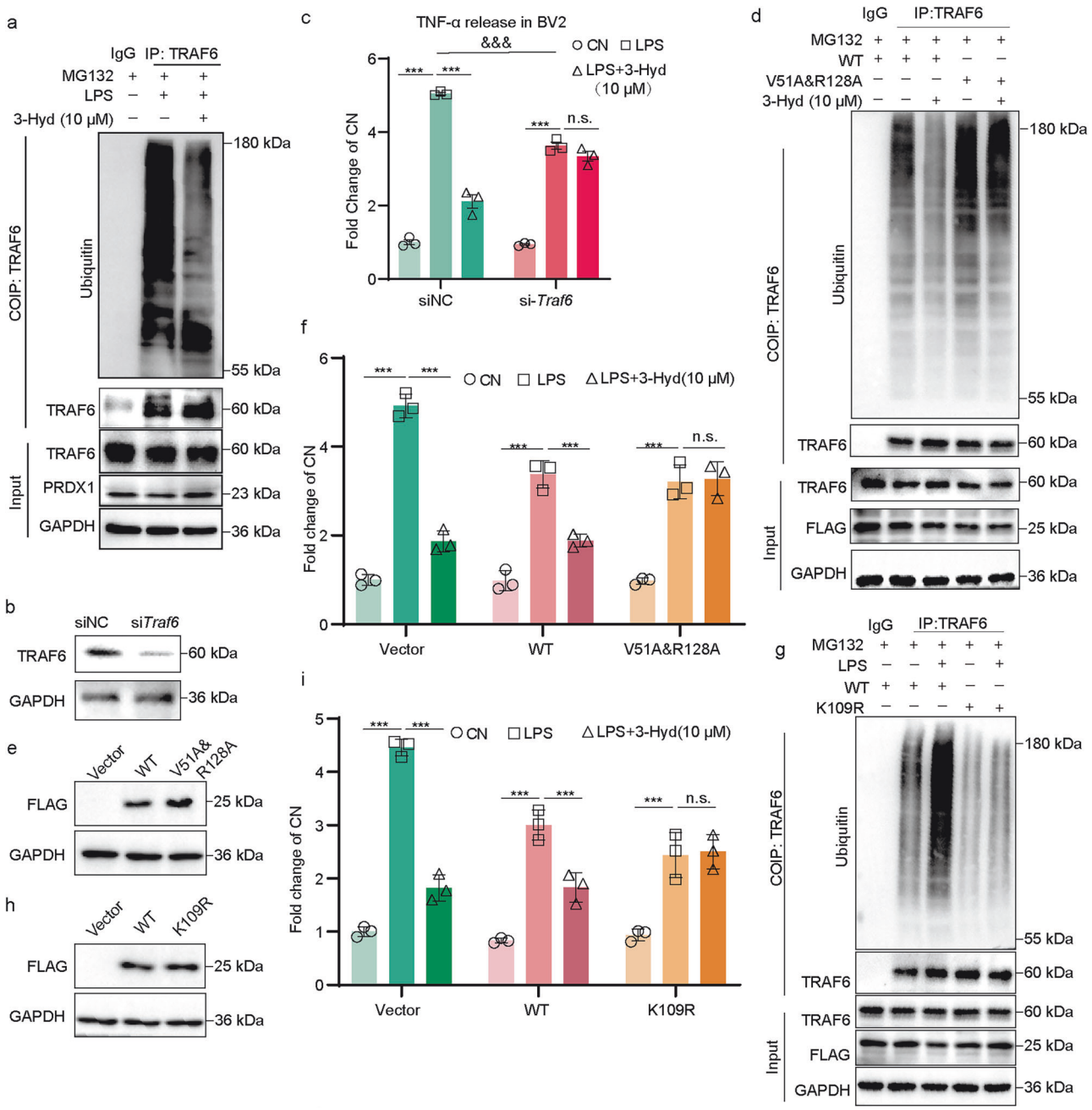


Fig. 7 3-Hyd attenuates neuroinflammation through the PRDX1-TRAF6 axis. a Representative Co-IP and Western blotting images evaluating the effect of 3-Hyd on overall TRAF6 ubiquitination levels in BV2 cells. Knockdown of endogenous *Traf6* in BV2 cells using siRNA. Representative Western blotting images of knockdown efficiency (**b**) and ELISA quantification of 3-Hyd's inhibitory effect on LPS-induced TNF-α release (**c**). **d** Representative Co-IP and Western blotting images detecting 3-Hyd's inhibitory effect on TRAF6 ubiquitination in BV2 cells overexpressing WT PRDX1 or the PRDX1$^{V51A\&R128A}$ double mutant (lacking 3-Hyd binding capacity). Overexpression of WT PRDX1 or PRDX1$^{V51A\&R128A}$ in BV2 cells. Representative Western blotting images of transfection efficiency (**e**) and ELISA quantification of 3-Hyd's effect on LPS-induced TNF-α release (**f**). **g** Representative Co-IP and Western blotting images detecting TRAF6 ubiquitination levels in BV2 cells overexpressing WT PRDX1 or its ubiquitination-resistant mutant (PRDX1^{K109R}). Overexpression of WT PRDX1 or PRDX1^{K109R} in BV2 cells to evaluate whether 3-Hyd exerts anti-inflammatory effects via the PRDX1 K109 residue. Representative Western blotting images of overexpression efficiency (**h**) and ELISA quantification of 3-Hyd's effect on LPS-induced TNF-α release (**i**). Data are presented as mean ± SD ($n = 3$/group). Statistical analyses were performed using two-way ANOVA followed by Sidak's multiple comparisons test (**c, f, i**). $^{***}P < 0.001$ *vs*. LPS group within the same transfection group; $^{\&\&\&}P < 0.001$ *vs*. siNC group within the LPS treatment group; n.s. (not significant).

DISCUSSION

In this study, we reveal for the first time that 3-hydroxydehydroleucodin (3-Hyd), a sesquiterpene constituent of Kudiezi injection (KDZ), serves as the key component responsible for its anti-neuroinflammatory effects. Through in vitro and in vivo models combined with comprehensive chemical biology techniques, we elucidated the pharmacological mechanism through which 3-Hyd:3-Hyd non-covalently targets and binds to the PRDX1 protein, specifically blocking the E3 ubiquitin ligase TRIM21-mediated K48-linked ubiquitination and degradation of PRDX1. The subsequently stabilized and accumulated PRDX1 inhibits the TRAF6-mediated NF-κB cascade,

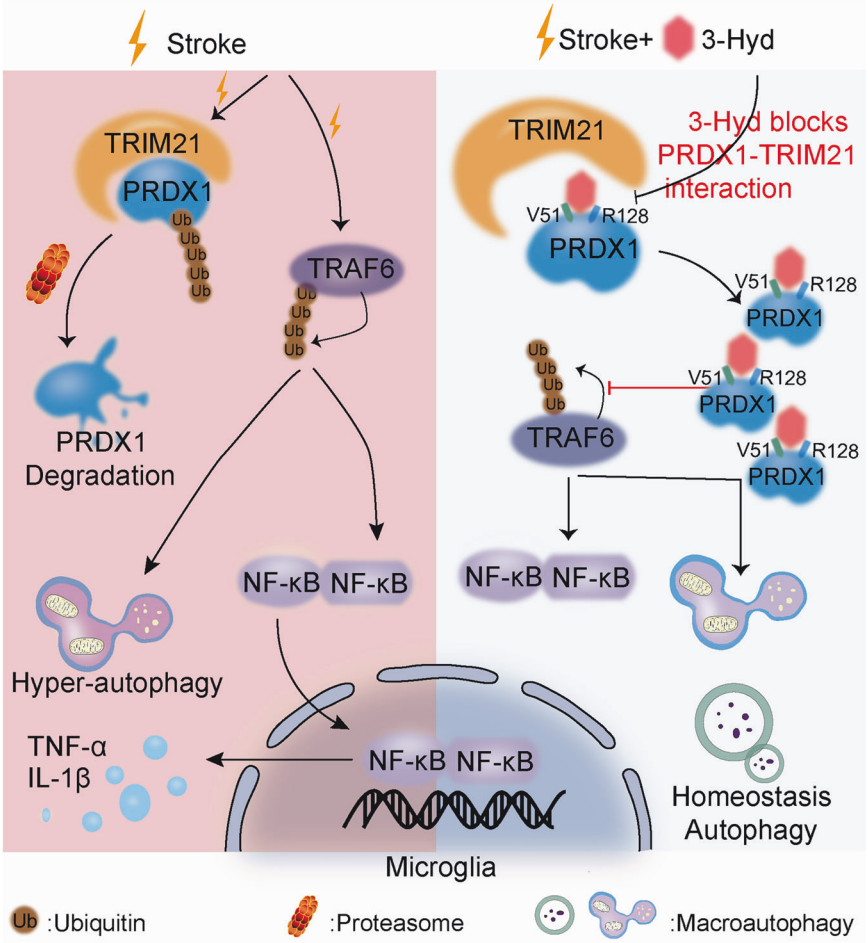


Fig. 8 Proposed scheme for 3-Hyd exhibiting anti-neuroinflammatory effects by targeting PRDX1 to block the TRIM21-PRDX1 interaction. During ischemia-induced microglial hyperactivation, TRAF6 activates the NF-κB signaling cascade and autophagic pathways, driving robust pro-inflammatory cytokine expression and excessive autophagic flux. Concurrently, PRDX1 undergoes accelerated proteasome degradation mediated by the E3 ubiquitin ligase TRIM21. 3-Hyd specifically binds to the V51 and R128 residues of PRDX1, physically disrupting the TRIM21-PRDX1 interaction and preventing the ubiquitin-dependent degradation of PRDX1. The stabilized PRDX1 subsequently suppresses TRAF6 ubiquitination, effectively restraining the microglial inflammatory response and excessive autophagy to ameliorate ischemic brain injury.

thus attenuating the inflammatory cascade and excessive autophagic activation in microglia (Fig. 8). This discovery not only clarifies the substance basis for the anti-ischemic effect of KDZ but also highlights the critical pathological significance of the TRIM21-PRDX1-TRAF6 regulatory axis in neuroinflammation for the first time and suggests that targeting the TRIM21-PRDX1 interaction is a promising strategy for the treatment of ischemic stroke.

Following ischemic stroke, damage-associated molecular patterns (DAMPs) released by necrotic cells rapidly trigger the innate immune system in the brain [63]. As the "first responders" of the central nervous system, the microglia and their excessive activation toward a pro-inflammatory phenotype (especially the expansion of the *Spp1*-high subpopulation) are the main driving forces that amplify the neuroinflammatory network and exacerbate secondary brain tissue injury [64]. Although traditional Chinese medicine (TCM) formulas, such as KDZ, have demonstrated synergistic protective advantages through multi-component, multi-target, and multi-pathway mechanisms in clinical practice—such as in previous reports indicating their ability to downregulate pro-inflammatory cytokines by modulating PDCD4/MAPK/NF-κB pathways [11]—the lack of a clear key substance basis has severely limited their translation into modernized targeted medicine. In parallel, our results confirm that the anti-inflammatory activity of the sesquiterpene lactone compound 3-Hyd is significantly superior to that of the other major components within KDZ. This provides highly persuasive cellular and molecular evidence for identifying the true active components of complex TCM systems and enabling precision-targeted interventions.

Discovering and validating the direct molecular targets of active compounds is the rate-limiting step in innovative drug development and represents the major breakthrough of this study. Previous studies have developed various PRDX1 inhibitors, such as celastrol [65] and glaucocalyxin A [66], which exert anti-tumor effects primarily by forming irreversible covalent bonds with the Cys-173 residue of PRDX1. However, such covalent binding often severely disrupts the overall redox homeostasis of normal cells, resulting in strongly toxic side effects. In stark contrast, our SPR and amino acid point mutation experiments verify that 3-Hyd does not target the key cysteine sites of PRDX1 (C52, C71, C83, and C173). Instead, it forms reversible noncovalent interactions with the V51 and R128 residues *via* hydrogen bonding. This unique binding mode ingeniously hinders steric hindrance, blocking the protein–protein interaction (PPI) between PRDX1 and TRIM21, thus specifically intervening in its ubiquitination. These findings clarify whether noncysteine-targeted binding influences the enzymatic function of PRDX1, providing a robust theoretical basis

for the development of other PRDX1-targeted small-molecule inhibitors. Additionally, conducting structure–activity relationship (SAR) analyses to design superior 3-Hyd derivatives with higher efficacy, enhanced targeting specificity, and lower toxicity is among our future objectives.

Autophagy acts as a "double-edged sword" in the progression of neuroinflammation [67, 68]. Moderate autophagy acts as an adaptive protective mechanism for cells, assisting in the clearance of damaged organelles and abnormal proteins. Conversely, under the intense stress of severe ischemia–reperfusion, the excessive activation of autophagy exacerbates cellular injury and the inflammatory storm. Our data corroborate this finding: tMCAO led to an abnormal increase in the expression of autophagy markers in microglia, whereas 3-Hyd intervention significantly reversed this trend. Tight dynamic crosstalk between autophagy and inflammation occurs in a pathological model of ischemic stroke. The remarkable neuroprotective efficacy of 3-Hyd both in vitro and in vivo is precisely attributed to its targeting of PRDX1, a "hub protein," which enables a "dual brake" and systemic correction of both the NF-κB inflammatory pathway and excessive autophagic flux.

Although this study elucidated in depth the molecular targeting mechanism of 3-Hyd, an extensive scope for exploration remains. First, to comprehensively evaluate the absolute contribution of 3-Hyd to the overall efficacy of KDZ, quantitative analysis technologies are needed in the future to determine its precise concentration in the original injection solution. Second, ischemic brain injury involves a complex communication network of multiple cell populations, including neurons, endothelial cells, and astrocytes. In the present study, only the mechanisms underlying microglia-mediated neuroinflammation were investigated. Given that microglial activation is a universal pathological hallmark across various neurological disorders, future investigations will expand the pharmacological validation of 3-Hyd into multiple microglia activation-involved disease models and diverse therapeutic time windows to explore its broader therapeutic spectrum. Future utilization of technologies, such as spatial transcriptomics, to delineate the multidimensional regulatory functions of PRDX1 in other cell subpopulations will further elucidate its biological landscape within the entire neural network. Finally, the identification of TRIM21 as the E3 ligase that mediates PRDX1 ubiquitination and the identification and characterization of the specific deubiquitinating enzymes (DUBs) responsible for PRDX1 modification during neuroinflammation constitute crucial final steps in mapping the dynamic equilibrium network of PRDX1 post-translational modifications, which is another important focus of our future work.

In this study, we revealed that 3-Hyd specifically targets pathologically activated microglia by acting on the PRDX1 protein. Mechanistically, 3-Hyd binds noncovalently to PRDX1, thus blocking its TRIM21-mediated K48-linked ubiquitination and subsequent proteasome degradation. The stabilization of PRDX1 effectively suppresses the TRAF6/NF-κB-driven inflammatory cascades and excessive autophagic activation in microglia. However, the phenotypic outcomes observed in our microglia-specific PRDX1 knockdown tMCAO model differ significantly from those reported in a previous global PRDX1 knockout (KO) study [23]. This apparent discrepancy is based on the distinct genetic strategies employed: global KO intrinsically deprives highly vulnerable neurons of their baseline antioxidant protection (inevitably exacerbating acute cell death), whereas our targeted knockdown approach strictly preserves the endogenous PRDX1 pool within the neuronal compartment. This biological distinction not only elucidates the differences in baseline infarct volumes but also highlights the critical importance of cell type-specific targeting in the development of precise therapeutic interventions for ischemic stroke. Ultimately, our findings reveal the TRIM21-PRDX1-TRAF6 signaling axis as a pivotal regulatory network in microglia-mediated neuroinflammation, suggesting that targeted disruption of the TRIM21-PRDX1 interaction is a viable translational strategy and that 3-Hyd is a highly promising compound for the treatment of cerebral ischemic stroke.

DATA AVAILABILITY

The bulk RNA-seq dataset has been deposited in the Gene Expression Omnibus (GEO) database under accession number GSE329344. The original, uncropped Western blotting images are provided in Supplementary Information. Other raw data supporting the conclusions of this article will be made available by the authors, without undue reservation, to any qualified researcher.

ACKNOWLEDGEMENTS

This work was supported by the National Key Research and Development Project (2024YFA0918500), the National Natural Science Foundation of China (U2102201, 32570462, 82174010), the Jiangsu Provincial Major Science and Technology Projects (SBG20250000118), the Xinjiang Uygur Autonomous Region Science and Technology Support Project (2024E02051), and the Double First-Class Project of China Pharmaceutical University (CPU2025CXY02). We sincerely thank Prof. Chunyong Ding (Shanghai Jiao Tong University) and Prof. Hao Zhang (Shanghai University of Traditional Chinese Medicine) for their generous support and assistance in conducting the PRDX1 enzymatic activity assay.

AUTHOR CONTRIBUTIONS

YH, LHH, and TP conceptualized the idea; KL, LW, ZC, YXQ, JHG, TTX, YL, and HH contributed to the investigation, methodology, formal analysis, validation and visualization of the experiment and data; YH, LHH, and TP administrated the project; YH, LHH, and TP supervised the study; KL and LW wrote the original manuscript draft; YH, LHH, and TP reviewed and edited the manuscript. All authors commented on and approved the manuscript.

ADDITIONAL INFORMATION

Supplementary information The online version contains supplementary material available at https://doi.org/10.1038/s41401-026-01922-6.

Competing interests: The authors declare no competing interests.

REFERENCES

1. The epidemiology and burden of cardiovascular diseases in countries of the Association of Southeast Asian Nations (ASEAN), 1990–2021: findings from the Global Burden of Disease Study 2021. Lancet Public Health 2025;10:e467-e79.
2. Rautalin I, Volovici V, Stark BA, Johnson CO, Kaprio J, Korja M, et al. Global, regional, and national burden of nontraumatic subarachnoid hemorrhage: the global burden of disease study 2021. JAMA Neurol. 2025;82:765–87.
3. Ho JP, Powers WJ. Contemporary management of acute ischemic stroke. Annu Rev Med. 2025;76:417–29.
4. Zhang M, Liu Q, Meng H, Duan H, Liu X, Wu J, et al. Ischemia-reperfusion injury: molecular mechanisms and therapeutic targets. Signal Transduct Target Ther. 2024;9:12–50.
5. Shi FD, Yong VW. Neuroinflammation across neurological diseases. Science. 2025;388:eadx0043.
6. Li W, Liao Y, Chen J, Kang W, Wang X, Zhai X, et al. Ischemia-reperfusion injury: a roadmap to precision therapies. Mol Asp Med. 2025;104:101382.
7. Wu J, Xu W, Su Y, Wang GH, Ma JJ. Targeting chaperone-mediated autophagy in neurodegenerative diseases: mechanisms and therapeutic potential. Acta Pharmacol Sin. 2025;46:816–28.
8. Tuo QZ, Zhang ST, Lei P. Mechanisms of neuronal cell death in ischemic stroke and their therapeutic implications. Med Res Rev. 2022;42:259–305.
9. Yang L, Li X, Zhao Y, Chen H, Wang C, Wu A, et al. NAT10 inhibition alleviates astrocyte autophagy by impeding ac4C acetylation of Timp1 mRNA in ischemic stroke. Acta Pharm Sin B. 2025;15:2575–92.
10. Xu L, Li C, Zhao C, Wang Z, Zhang Z, Shu X, et al. Shionone protects against cerebral ischemic injury by alleviating microglia-mediated neuroinflammation. Chin J Nat Med. 2025;23:471–9.
11. Sun M, Han G, Yu H, Wang F. Kudiezi injection attenuates apoptosis and neuroinflammation for ameliorating angiogenesis via miR-21/PDCD4/NF-κB axis in MCAO/reperfusion rats. J Ethnopharmacol. 2025;350:120066.
12. Liu X, Zhang X, Wang F, Liang X, Zeng Z, Zhao J, et al. Improvement in cerebral ischemia-reperfusion injury through the TLR4/NF-κB pathway after Kudiezi injection in rats. Life Sci. 2017;191:132–40.

13. Xie R, Liu Z, Lin Z, Shi P, Chen B, Li S, et al. Potential mechanism of action of *Ixeris sonchifolia* extract injection against cardiovascular diseases revealed by a combination of HPLC-Q-TOF-MS, virtual screening, and systems pharmacology approach. RSC Adv. 2020;10:38497–504.
14. Liu SY, Cai W, Wang F, Liu Y, Shang ZP, Zhang XP, et al. UHPLC-LTQ-Orbitrap-based metabolomics coupled with metabolomics pathway analysis method for exploring the protection mechanism of Kudiezi injection in a rat anti-ischemic cerebral reperfusion damage model. Chin J Nat Med. 2017;15:955–60.
15. Liu RR, Zhang XP, Wang F, Shang ZP, Wang F, Liu Y, et al. Rapid screening and identification of sesquiterpene lactones in Kudiezi injection based on high-performance liquid chromatography coupled with linear ion trap-orbitrap mass spectrometry. Chin J Nat Med. 2018;16:150–60.
16. Liu K, Wang L, Pang T. Research progress of small-molecule natural medicines for the treatment of ischemic stroke. Chin J Nat Med. 2025;23:21–30.
17. Wang Y, Yao J, Sui Y, Jiang H, Ma B, Lai S, et al. HerbSyner_Finder: a network community-based model for identifying synergistic combinations from herbal medicines and complex systems. Targetome. 2026;2:e012.
18. Ge MM, Zhang XM, Xu C, Miao CH, Liao QW. Peroxiredoxins in the central nervous system: implications for chronic pain and anaesthetic-induced neurotoxicity management. Redox Biol. 2025;87:103898.
19. Jia C, Ke-Hong C, Fei X, Huan-Zi D, Jie Y, Li-Ming W, et al. Decoy receptor 2 mediation of the senescent phenotype of tubular cells by interacting with peroxiredoxin 1 presents a novel mechanism of renal fibrosis in diabetic nephropathy. Kidney Int. 2020;98:645–62.
20. Yang T, Zhang S, Nie K, Cheng C, Peng X, Huo J, et al. ZNF207-driven PRDX1 lactylation and NRF2 activation in regorafenib resistance and ferroptosis evasion. Drug Resist Update. 2025;82:101274.
21. Chen H, Zhao J, Kang Y, Wang S, Qin D, Yu L, et al. PFGA12 ameliorates hypoxic-ischemic brain injury by directly regulating PRDX1 and inhibiting ferroptosis. Biochem Pharmacol. 2025;242:117307.
22. Liu S, Wu Q, Xu C, Wang L, Wang J, Liu C, et al. Ischemic postconditioning regulates new cell death mechanisms in stroke: disulfidptosis. Biomolecules. 2024;14:1390–409.
23. Kim S, Lee W, Jo H, Sonn SK, Jeong SJ, Seo S, et al. The antioxidant enzyme Peroxiredoxin-1 controls stroke-associated microglia against acute ischemic stroke. Redox Biol. 2022;54:102347.
24. Guan X, Zhu S, Song J, Liu K, Liu M, Xie L, et al. Microglial CMPK2 promotes neuroinflammation and brain injury after ischemic stroke. Cell Rep Med. 2024;5:101522.
25. Li Z, Liu B, Lambertsen KL, Clausen BH, Zhu Z, Du X, et al. USP25 inhibits neuroinflammatory responses after cerebral ischemic stroke by deubiquitinating TAB2. Adv Sci. 2023;10:e2301641.
26. Robertson KV, Rodriguez AS, Cartailler JP, Shrestha S, Schleh MW, Schroeder KR, et al. Knockdown of the microglial iron import gene, Slc11a2, worsens cognitive function and alters the microglial transcriptional landscape in a sex-specific manner in the APP/PS1 model of Alzheimer's disease. J Neuroinflammation. 2024;21:238.
27. Schuhmann MK, Stoll G, Bieber M, Vögtle T, Hofmann S, Klaus V, et al. CD84 links T-cell and platelet activity in cerebral thrombo-inflammation in acute stroke. Circ Res. 2020;127:1023–35.
28. Navarro S, Talucci I, Göb V, Hartmann S, Beck S, Orth V, et al. The humanized platelet glycoprotein VI Fab inhibitor EMA601 protects from arterial thrombosis and ischaemic stroke in mice. Eur Heart J. 2024;45:4582–97.
29. Du LD, Fang C, Wang YQ, Feng ZY, Abiola OF, Gao ZL, et al. MMP-9 inhibitor SB-3CT improves neurological outcomes in ischemic stroke mice by modulating astrocytic lipid metabolism. Acta Pharmacol Sin. 2025;46:2120–35.
30. Qian Y, Yang L, Chen J, Zhou C, Zong N, Geng Y, et al. SRGN amplifies microglia-mediated neuroinflammation and exacerbates ischemic brain injury. J Neuroinflammation. 2024;21:35.
31. Rao Y, Du S, Yang B, Wang Y, Li Y, Li R, et al. NeuroD1 induces microglial apoptosis and cannot induce microglia-to-neuron cross-lineage reprogramming. Neuron. 2021;109:4094–108.e5.
32. Chen D, Wang C, Chen X, Li J, Chen S, Li Y, et al. Brain-wide microglia replacement using a nonconditioning strategy ameliorates pathology in mouse models of neurological disorders. Sci Transl Med. 2025;17:eads6111.
33. Song JQ, Shen LJ, Wang HJ, Liu QB, Ye LB, Liu K, et al. Discovery of a Balasubramide derivative with tissue-specific anti-inflammatory activity against acute lung injury by targeting VDAC1. Adv Sci. 2024;11:e2410550.
34. Hsieh MH, Chen PC, Hsu HY, Liu JC, Ho YS, Lin YJ, et al. Surfactant protein D inhibits lipid-laden foamy macrophages and lung inflammation in chronic obstructive pulmonary disease. Cell Mol Immunol. 2023;20:38–50.
35. Gao CL, Song J, Wang H, Shang Q, Guan X, Xu G, et al. The PGAM5-NEK7 interaction is a therapeutic target for NLRP3 inflammasome activation in colitis. Acta Pharm Sin B. 2025;15:349–70.
36. Gao CL, Song JQ, Yang ZN, Wang H, Wu XY, Shao C, et al. Chemoproteomics of marine natural product naamidine J unveils CSE1L as a therapeutic target in acute lung injury. J Am Chem Soc. 2024;146:28384–97.
37. Ruan Y, Zhu X, Shen J, Chen H, Zhou G. Mechanism of nicotiflorin in San-Ye-Qing rhizome for anti-inflammatory effect in ulcerative colitis. Phytomedicine. 2024;129:155564.
38. Hou CY, Suo YH, Lv P, Yuan HF, Zhao LN, Wang YF, et al. Aristolochic acids-hijacked p53 promotes liver cancer cell growth by inhibiting ferroptosis. Acta Pharmacol Sin. 2025;46:208–21.
39. Li XJ, Huang KX, Wang KX, Liu R, Wang DC, Liang YR, et al. Design, synthesis, and antitumor activity of novel thioheterocyclic nucleoside derivatives by suppressing the c-MYC pathway. Acta Pharmacol Sin B. 2025;15:3685–707.
40. Tan W, Wei X, Li C, Wei H, Yu F, Shen X, et al. Sanguinarine triggers apoptosis and ferroptosis synchronously by directly binding BiP in lung squamous cell carcinoma. Chin J Nat Med. 2026;24:427–39.
41. Li Y, Zhu Y, Shang FF, Xu L, Jiang D, Sun B, et al. Discovery of urea derivatives of celastrol as selective peroxiredoxin 1 inhibitors against colorectal cancer cells. J Med Chem. 2024;67:7176–96.
42. Forli S, Huey R, Pique ME, Sanner MF, Goodsell DS, Olson AJ. Computational protein-ligand docking and virtual drug screening with the AutoDock suite. Nat Protoc. 2016;11:905–19.
43. Bugnon M, Röhrig UF, Goullieux M, Perez MAS, Daina A, Michielin O, et al. SwissDock 2024: major enhancements for small-molecule docking with attracting cavities and AutoDock Vina. Nucleic Acids Res. 2024;52:W324–W32.
44. Liu K, Hao Z, Zheng H, Wang H, Zhang L, Yan M, et al. Repurposing of rilpivirine for preventing platelet β3 integrin-dependent thrombosis by targeting c-Src active autophosphorylation. Thromb Res. 2023;229:53–68.
45. Kong X, Lyu W, Lin X, Lin C, Feng H, Xu L, et al. Itaconate alleviates anesthesia/surgery-induced cognitive impairment by activating Nrf2-dependent anti-neuroinflammation and neurogenesis via the gut-brain axis. J Neuroinflammation. 2024;21:104.
46. Wang Z, Lipshutz A, Martínez de la Torre C, Trzeciak AJ, Liu ZL, Miranda IC, et al. Early-life high fructose impairs microglial phagocytosis and neurodevelopment. Nature. 2025;644:759–68.
47. Egger B, van Giesen L, Moraru M, Sprecher SG. In vitro imaging of primary neural cell culture from Drosophila. Nat Protoc. 2013;8:958–65.
48. Hao H, Kirchhoff F. Navigating drug discovery with targetome. Targetome. 2025;1:e001.
49. Min Y, Kim MJ, Lee S, Chun E, Lee KY. Inhibition of TRAF6 ubiquitin-ligase activity by PRDX1 leads to inhibition of NFKB activation and autophagy activation. Autophagy. 2018;14:1347–58.
50. Liang YY, Khalid K, Le HV, Teo HMV, Raitelaitis M, Gerault MA, et al. MS CETSA deep functional proteomics uncovers DNA repair programs leading to gemcitabine resistance. Nat Commun. 2025;16:4234.
51. Špringer T, Bocková M, Slabý J, Sohrabi F, Čapková M, Homola J. Surface plasmon resonance biosensors and their medical applications. Biosens Bioelectron. 2025;278:117308.
52. Gao W, Yang X, Li Q, Liu Y, Huang W, Xia X, et al. Covalent affibody-molecular glue drug conjugate nanoagent for proximity-enabled reactive therapeutics. Adv Sci. 2025;12:e2412273.
53. Kim G, Grams RJ, Hsu KL. Advancing covalent ligand and drug discovery beyond cysteine. Chem Rev. 2025;125:6653–84.
54. Pohl C, Dikic I. Cellular quality control by the ubiquitin-proteasome system and autophagy. Science. 2019;366:818–22.
55. Cruz Walma DA, Chen Z, Bullock AN, Yamada KM. Ubiquitin ligases: guardians of mammalian development. Nat Rev Mol Cell Biol. 2022;23:350–67.
56. Pla-Prats C, Thomä NH. Quality control of protein complex assembly by the ubiquitin-proteasome system. Trends Cell Biol. 2022;32:696–706.
57. Ebadi P, Stratton CM, Olsen SK. E3 ubiquitin ligases in signaling, disease, and therapeutics. Trends Biochem Sci. 2025;50:960–76.
58. Tracz M, Bialek W. Beyond K48 and K63: non-canonical protein ubiquitination. Cell Mol Biol Lett. 2021;26:1–17.
59. Cai C, Tang YD, Zhai J, Zheng C. The RING finger protein family in health and disease. Signal Transduct Target Ther. 2022;7:300.
60. Wang J, Wang Q, Li X, Cai Q, Bi Y, Xu C, et al. Emerging roles of TRIM in metabolic regulation. Metabolism. 2025;174:156394.
61. Alomari M. TRIM21 - A potential novel therapeutic target in cancer. Pharmacol Res. 2021;165:105443.
62. Wang W, Wang Y, Wang F, Xie G, Liu S, Li Z, et al. Gastrodin regulates the TLR4/TRAF6/NF-κB pathway to reduce neuroinflammation and microglial activation in an AD model. Phytomedicine. 2024;128:155518.
63. Fan H, Tang HB, Chen Z, Wang HQ, Zhang L, Jiang Y, et al. Inhibiting HMGB1-RAGE axis prevents pro-inflammatory macrophages/microglia polarization and affords neuroprotection after spinal cord injury. J Neuroinflammation. 2020;17:295.

64. Lan Y, Zhang X, Liu S, Guo C, Jin Y, Li H, et al. Fate mapping of Spp1 expression reveals age-dependent plasticity of disease-associated microglia-like cells after brain injury. Immunity. 2024;57:349–63.e9.
65. Xu H, Zhao H, Ding C, Jiang D, Zhao Z, Li Y, et al. Celastrol suppresses colorectal cancer via covalent targeting peroxiredoxin 1. Signal Transduct Target Ther. 2023;8:51.
66. Wang Y, Luo W, Shen S, Zhuang Y, Zhu Y, Liu Y, et al. Glaucocalyxin A induces autophagy-mediated ferroptosis by targeting PRDX1 and TXNRD1 proteins in non-small cell lung cancer. Phytomedicine. 2025;148:157280.
67. Gao C, Jiang J, Tan Y, Chen S. Microglia in neurodegenerative diseases: mechanism and potential therapeutic targets. Signal Transduct Target Ther. 2023;8:359.
68. Hwang I, Kim BS, Lee HY, Cho SW, Lee SE, Ahn JY. PA2G4/EBP1 ubiquitination by PRKN/PARKIN promotes mitophagy, protecting against neuronal death in cerebral ischemia. Autophagy. 2024;20:365–79.

Publisher's note Springer Nature remains neutral with regard to jurisdictional claims in published maps and institutional affiliations.

Springer Nature or its licensor (e.g. a society or other partner) holds exclusive rights to this article under a publishing agreement with the author(s) or other rightsholder(s); author self-archiving of the accepted manuscript version of this article is solely governed by the terms of such publishing agreement and applicable law.